Computation of solitary wave profiles described by a Hamiltonian model for surface waves

Eindverslag van de ontwerpersopleiding
WISKUNDE VOOR DE INDUSTRIE

Final report of the postgraduate programme
MATHEMATICS FOR INDUSTRY

COMPUTATION OF SOLITARY WAVE PROFILES DESCRIBED BY A HAMILTONIAN MODEL FOR SURFACE WAVES

Drs T.J.G. Zwartkruis

University supervisor: Dr J. Molenaar,
Technische Universiteit, Eindhoven

Industrial supervisor: Drs A.C. Radder,
Rijkswaterstaat, Tidal Waters Devision, The Hague (NL)

March 1991

CIP data, Koninklijke Bibliotheek, Den Haag

Zwartkruis, T.J.G.

Computation of solitary wave profiles described by a Hamiltonian model for surface waves / T.J.G. Zwartkruis; [ill. by the author]. - Eindhoven: Instituut Vervolgopleidingen, Technische Universiteit Eindhoven. - Ill.
With suppl.
Final report of the postgraduate programme Mathematics for industry.
With index, ref.
ISBN 90-5282-121-6 bound

Subject heading: wave motions

ISBN 90 5282 121 6

ABSTRACT

An explicit Hamiltonian formulation for two-dimensional wave motion is considered. A straightforward approximation of the Hamiltonian density in shallow water is examined by looking at the limiting case of solitary waves. For a quasi steady state, the governing equations can be reduced to a nonlinear integral equation of Hammerstein type. Numerical calculations yield solitary wave solutions to this nonlinear integral equation.

After this, three possible approaches towards a numerical treatment of the governing equations are mentioned. The first one is implemented in a simple numerical scheme for a model situation. Numerical experiments are carried out to gain some insight into the behaviour of the scheme. The results of these experiments are presented.

PREFACE

This report is the result of a six months lasting final project of the postgraduate course "Mathematics for Industry" at the Eindhoven University of Technology.

The project was carried out at the Tidal Waters Division of Rijkswaterstaat in The Hague. Rijkswaterstaat (RWS) is part of the Ministry of Transport and Public Works in The Netherlands and is responsible for the construction and maintenance of both the dry and wet infrastructure in The Netherlands. The Tidal Waters Division (TWD) is an advising organization for the regional directories of RWS that take care of the wet infrastructure (e.g., dykes), cooperates in large projects such as The Delta Works and, finally, carries out research in order to keep the level of knowledge in the organization up to date.

An example of the last objective is the development of a computational model for the description of sea waves approaching the coast. More specifically, TDW is interested in the evolution of the energy spectrum of sea waves in the area near the coast (0-20m seawards). This project is part of this research.

I thank Drs.A.C.Radder(TDW,RWS) and Dr.J.Molenaar(T.U.E.) for their enthusiastic help and advices, and Dr.A.Reusken(T.U.E.) for useful comments during the writing of this report.

The Hague, February 1991,
Theo Zwartkruis.

CONTENTS

1 INTRODUCTION

This section sketches the general background of surface water waves research. It also contains a description of the global objectives of the research presented in this report.

1.1 Background.

Water waves can develop in all circumstances where the surface of the water is free to move. Many different types of waves are distinguished. Most directly experienced by mankind are wind waves and swell in the sea, generated by local and distant storms. Tsunamis, caused by large submarine earthquakes, occur less frequently but have occasionally disastrous consequences. Other types of wave motion are tides, seiches, bores and internal waves. Other causes for the development of waves are human activities (ship motion, explosion), gravity and earth rotation.

Knowledge of the behaviour of surface water waves is important for a variety of reasons. For example, naval architects need to know the dynamics of waves when they design ships. Coastal engineers and people in offshore industries need to know the forces on structural parts of coastal and offshore structures such as dykes and oil rigs. Also, the knowledge is indispensable in the evaluation and prediction of the evolution of natural coastlines.

In the Netherlands, partially situated below sea level, a good understanding of the effects of sea waves on both natural and artificial barriers against the sea, such as dunes and dykes, is of vital importance. Even though the most vulnerable parts of the country are nowadays protected by the Delta Works, the expected sea level rise and the decreasing funds for the maintenance of protecting barriers make the prediction of the harm that sea waves can cause still of current interest.

It is common to follow a stochastic approach to describe the effects of sea waves. However, such a stochastic approach often benefits by incorporation of a deterministic description of the behaviour of waves. Numerous mathematical models have been developed during the last two centuries to describe water waves in various circumstances. Many results have already been obtained, but it is still very difficult to give a good description of the evolution of the energy spectrum of sea waves approaching the coast in the area of 0-20m seawards. In this area various physical processes may influence the wave field, e.g., shoaling and energy dissipation due to wave breaking. A

complete modeling of these effects is not only very hard, most of the time it leads to problems that are difficult to solve. As a result, one often chooses a simpler approach.

A lot of results has been obtained by considering those descriptions which assume the wave motion to be irrotational and the fluid to be inviscid and incompressible. In spite of these restrictions models are encountered which are not analytically tractable yet. So, further assumptions are made. Two main groups of theories can be distinguished, viz. Stokes wave theories and shallow water wave theories. Stokes wave theories are used to describe short waves, i.e., waves satisfying the condition that the ratio of the mean water depth and wave length $h/L \geq 1/10$. Shallow water theories are used to describe longer waves, i.e., waves satisfying the condition that $h/L \ll 1$.

In order to describe waves that approach the coast it is necessary to have a model which combines both deep and shallow water effects. Several attempts for such a unified theory have been made in the past, e.g., by Whitham(1967,1974), Witting(1984) and Murray(1988). In Radder(1991) such a model is developed based on a Hamiltonian formulation of the water wave problem.

1.2 Objectives.

The starting point for this research is the explicit Hamiltonian formulation for two-dimensional wave motion developed by Radder(1991). In this theory a straightforward approximation of the Hamiltonian density seems to lead to a reliable description of the shallow water case. The validity of this approximation will be examined by looking at the limiting case of solitary waves for which extensive information is available in the literature. After that, attention is paid to rewrite the governing equations in such a form that they can be tackled numerically.

2 THE MATHEMATICAL MODEL, ITS PROPERTIES AND THE PROBLEM

This section starts with two equivalent formulations of the water wave problem, namely the classical formulation and the Hamiltonian one. The second formulation is explicitly worked out for two-dimensional wave motion in Radder(1991) and the main properties of this description are summarized here. Finally, the problems tackled in this research are described.

2.1 The classical formulation.

The water wave problem is the problem to describe the behaviour of water, subject to the restoring forces of gravity and surface tension.

In the classical formulation of the problem (cf. Mei(1983)) a fluid in a constant gravitational field is considered. The fluid is assumed to be incompressible, inviscid and of uniform density. The flow is taken to be irrotational. In this case a velocity potential $\Phi(x,y,z,t)$ can be introduced. The unknown Φ satisfies the Laplace equation

$$\frac{\partial^2\Phi}{\partial x^2} + \frac{\partial^2\Phi}{\partial y^2} + \frac{\partial^2\Phi}{\partial z^2} = 0. \tag{2.1}$$

Let $\zeta(x,y,t)$ denote the surface elevation, $h(x,y)$ the position of the bottom, ∇ the horizontal gradient operator $(\frac{\partial}{\partial x},\frac{\partial}{\partial y})$, g the acceleration of gravity and σ the coefficient of surface tension (see also Figure 2.1).

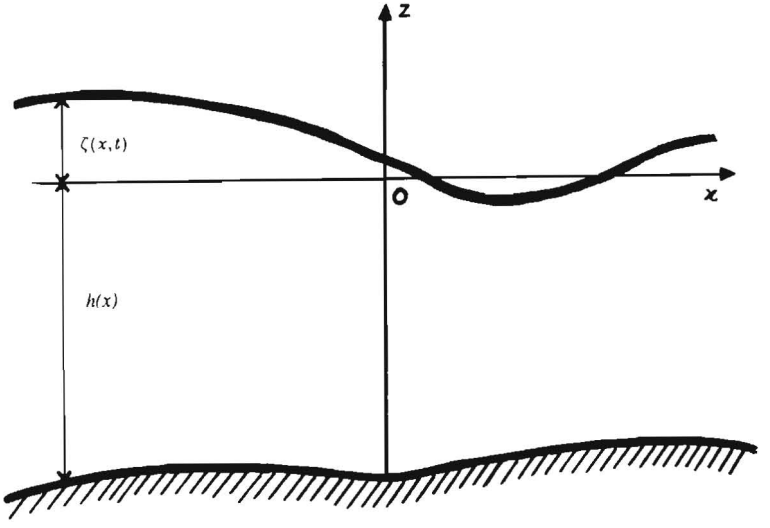

Figure 2.1. Water on top of a variable bottom (two-dimensional case).

The following boundary conditions hold:

--- the normal velocity of the fluid must vanish on the bottom, i.e.,

$$(2.2) \qquad \nabla h.\nabla\Phi + \frac{\partial\Phi}{\partial z} = 0 \qquad \text{at } z = -h(x,y),$$

--- the normal velocity of the free surface must equal the normal velocity of the fluid at the free surface, i.e.,

$$(2.3) \qquad \frac{\partial\zeta}{\partial t} + \nabla\zeta.\nabla\Phi = \frac{\partial\Phi}{\partial z} \qquad \text{at } z = \zeta(x,y,t),$$

--- there is an equilibrium of forces at the free surface, i.e.,

$$(2.4) \qquad \frac{\partial\Phi}{\partial t} + g\zeta + \frac{1}{2}\left[(\nabla\Phi)^2 + \left(\frac{\partial\Phi}{\partial z}\right)^2\right] - \sigma\nabla.\left(\frac{\nabla\zeta}{\sqrt{1+(\nabla\zeta)^2}}\right) = 0$$

$$\text{at } z = \zeta(x,y,t).$$

The main difficulty in this formulation is the nonlinearity of the boundary conditions at the unknown free surface.

For small amplitude waves, i.e., waves with a small wave slope (*2π×amplitude/wavelength*), a linearization of the formulae can be accomplished and much is known of this in the literature. However, inclusion of nonlinear effects is necessary for the description of steeper waves.

With the increase of digital computing possibilities many results have been obtained by means of a direct numerical treatment of the equations mentioned above (cf. Fenton&Rienecker(1982), Longuet-Higgins&Cokelet(1978)). Nevertheless, it takes quite some effort to handle the nonlinear boundary conditions on the unknown surface and the computational costs are high. Therefore, it is still worthwhile to look for analytical results, e.g., by means of an alternative description of the problem.

2.2 The Hamiltonian formulation.

In the Hamiltonian theory the total energy of the fluid is considered (cf. Broer(1974), Miles(1977)). Again a fluid in a constant gravitational field is considered. Again the fluid is assumed to be incompressible, inviscid and of uniform density, and again the flow is taken to be irrotational.

Let V denote the potential energy density, T the kinetic energy density and $H=V+T$ the Hamiltonian density. Then, the total energy of the fluid $\mathcal{H}$ is given by (omitting the uniform density)

$$(2.5)\qquad \mathcal{H} = \iint H dxdy = \iint (V+T)dxdy =$$

$$\iint \left\{ \tfrac{1}{2} g\zeta^2 + \sigma\left(\sqrt{1+(\nabla\zeta)^2}\,-1\right) + \tfrac{1}{2}\int_{-h}^{\zeta} \left[(\nabla\Phi)^2 + \left(\frac{\partial\Phi}{\partial z}\right)^2 \right] dz \right\} dxdy.$$

Now, it is known from the literature that ζ and $\phi=\Phi(x,y,\zeta,t)$ are canonical variables in Hamilton's sense where $\mathcal{H}(\zeta,\phi)$ is the corresponding Hamiltonian functional (cf. Zakharov(1968), Broer(1974), Broer&VanGroesen& Timmers(1976)).

The canonical equations

$$(2.6)\qquad \frac{\partial\zeta}{\partial t} = \frac{\delta\mathcal{H}}{\delta\phi}, \qquad \frac{\partial\phi}{\partial t} = -\frac{\delta\mathcal{H}}{\delta\zeta},$$

(where δ denotes the variational derivative) are equivalent to *(2.3)* and *(2.4)* with *(2.1)* and *(2.2)* as constraints. These equations have to be solved for the unknown surface elevation ζ and the unknown velocity potential at the free surface ϕ.

Advantages of the Hamiltonian formulation are the relative simplicity and the numerically stable behaviour of the canonical equations for any approximate positive definite Hamiltonian density (cf. Broer(1974,1975)). The disadvantage is the difficulty to express the kinetic energy density T explicitly as a functional of ζ and ϕ. This is necessary in order to apply *(2.6)*. In Radder(1991) this difficulty is solved for the two-dimensional problem in the *(x,z)*-plane with a constant horizontal bottom. The main results of Radder(1991) are summarized in the next two subsections.

2.3 Explicit formulation of the two-dimensional problem.

When the flow is two-dimensional, i.e., there is no dependency on, say, the space variable y, an elaborate derivation shows that for a horizontal bottom

$$(2.7)\qquad T = \tfrac{1}{2}\int_{-\infty}^{\infty} \phi_x \phi_{x'} R_\varepsilon(x,x';\eta)dx',$$

where the symmetric function R_ε is given by

$$(2.8)\qquad R_\varepsilon(x,x';\eta) = -\tfrac{1}{\pi} ln\left(tanh\left\{ \tfrac{\pi}{4} \left| \int_{x}^{x'} \frac{1}{(1+\varepsilon(r,t))\eta(r,t)} dr \right| \right\} \right)$$

and η, ε are functions defined by

(2.9) $\eta(x,t) = h + \zeta(x,t)$

$$\varepsilon(x,t) = -\tfrac{1}{3}(\eta_x^2+\eta\eta_{xx}) -$$

$$\tfrac{1}{45}(-9\eta_x^4-6(4\eta_x^2+\eta\eta_{xx})\eta\eta_{xx}+2\eta^2\eta_x\eta_{xxx}+\eta^3\eta_{xxxx}) - \ldots$$

2.4 Special cases.

For some special cases the results above are examined more closely. In these cases the surface tension is neglected. The formulation in §§*2.2*, *2.3* reduces to well-known theory for deep and shallow water.

Let λ denote a typical wave length, $k=2\pi/\lambda$ a typical wave number and a a typical amplitude. The typical wave steepness is then ka.

For deep water, i.e., $kh\to\infty$, Stokes theory is appropriate, $\eta\approx h$ and a simple scaling yields that $\varepsilon=O(ka)$. It is shown that the Hamiltonian formulation with

(2.10) $$R_\varepsilon(x,x';h) = -\tfrac{1}{\pi} ln\left(tanh\left\{\tfrac{\pi}{4h}\Big|_x\int^{x'}\tfrac{1}{(1+\varepsilon)}dr\Big|\right\}\right)$$

provides a correct description of third order Stokes waves in deep water.

For shallow water, i.e., $kh\ll 1$, $\varepsilon=O(k^2ha)$ and ε is put to zero such that *(2.8)* reduces to

(2.11) $$R_0(x,x';\eta) = -\tfrac{1}{\pi} ln\left(tanh\left\{\tfrac{\pi}{4}\Big|_x\int^{x'}\tfrac{1}{\eta}dr\Big|\right\}\right).$$

If $O(k^2h^2)=O(a/h)\ll 1$ Boussinesq theory is appropriate and it is shown that the present formulation of Hamiltonian density reduces to a result found by Broer(1975).

Also for shallow water, the limiting case of the solitary wave of finite amplitude is considered. The parameter $\alpha=a/h$ is not assumed to be small in this case. The canonical equations are now given by

(2.12) $$\frac{\partial\zeta}{\partial t} = \frac{1}{\pi}\frac{\partial}{\partial x}\int_{-\infty}^{\infty}\phi_{x'} ln\left(tanh\left\{\tfrac{\pi}{4}\Big|_x\int^{x'}\tfrac{1}{\eta}dr\Big|\right\}\right)dx' ,$$

(2.13) $$\frac{\partial\phi}{\partial t} = -g\zeta - \frac{1}{2\eta^2}\int_{-\infty}^{x}\int_{x}^{\infty}\frac{\phi_{x'}\phi_{x''}}{sinh\left(\tfrac{\pi}{2}\Big|_{x'}\int^{x''}\tfrac{1}{\eta}dr\Big|\right)}dx''dx' .$$

Broer's result leads to canonical equations which are expected to be

valid only for small α. These equations have solitary wave solutions and there exists an upper bound for the amplitude of the solutions. Other theories also predict the existence of a highest solitary wave. Such a wave would exhibit a sharp crest with an interior angle of 120° and a maximum value of α, $\alpha_{max}=5/6\approx 0.833$. Therefore, it is very interesting to see if *(2.12)* and *(2.13)* have solitary wave solutions and if so, if these solutions include a highest solitary wave.

Finally, Radder(1991) conjectures that the method can be made approximately valid for waves in water on top of an uneven bottom by replacing h by $h(x)$ in the function R_{ε}.

2.5 Problem description.

The main objective of the research is to check the validity and usefulness of the description in §§*2.2*, *2.3* for shallow water, i.e., the case in which the function ε is put to zero. In this context, the limiting case of the solitary wave deserves special attention because it is extensively studied in the literature. In addition, a first approach towards a numerical scheme for the equations of motion will be made.

More specifically, the following questions are posed:

(1) Do the equations *(2.12)* and *(2.13)* have solitary wave solutions?

(2) If *(2.12)* and *(2.13)* do have solitary wave solutions, does a highest solitary wave exist with a sharp crest, an interior angle of 120° and a maximum height of 0.833?

(3) What kind of numerical scheme is appropriate for the equations *(2.12)* and *(2.13)*?

(4) Can the model also be used for a bottom with a small obstacle?

3 SOLITARY WAVE SOLUTIONS

This section starts with some introductory remarks on the phenomenon of the solitary wave. Then it is shown that the canonical equations *(2.12)* and *(2.13)*, which possibly have solitary wave solutions, can be reduced to a nonlinear integral equation of Hammerstein type for the unknown surface profile ζ. Numerical calculations yield approximate solutions to this integral equation. These approximate solutions can indeed be interpreted to be solitary waves but they do not include a highest solitary wave as a special case. A comparison with results in the literature is made.

3.1 The solitary wave.

A solitary wave is a wave consisting of a single hump of constant shape and moving with constant speed. John Scott Russell discovered and named it in 1834 and about forty years later Boussinesq and Rayleigh were the first to find theoretical results for this phenomenon. More recently, scientific interest stems from the discovery that many nonlinear equations, e.g., the Korteweg-deVries equation, have solitary wave solutions.

The essential property of the solitary wave is the perfect balance between nonlinearity and dispersion. Nonlinearity tends to steepen the wave front in consequence of the increase of wave speed with amplitude, and dispersion, i.e., the decrease of wave speed of a spectral component with increasing wave number, tends to spread the wave front.

Experiments show that waves exhibit a maximum height. Stokes conjectured in 1880 that the highest-possible steady wave would be characterized by sharp crests. The fluid velocity at the crest must then necessarily vanish in the frame of reference in which the flow is steady. Stokes also demonstrated that such a sharp crest would have to enclose an angle of 120°.

The maximal possible height of a solitary wave in a channel of constant depth h is still not known exactly. One of the most recent results is a maximum value of amplitude A over depth $\alpha_{max}=(A/h)_{max}=0.83322$ (cf. Hunter&VandenBroeck(1983)).

3.2 The quasi steady state and dimensionless equations.

For convenience, equations *(2.12)* and *(2.13)* are repeated here:

$$(3.1)\qquad \frac{\partial\zeta}{\partial t} = \frac{1}{\pi}\frac{\partial}{\partial x}\int_{-\infty}^{\infty}\phi_{x'}\,ln\left(tanh\left\{\frac{\pi}{4}\Big|\int_{x}^{x'}\frac{1}{\eta}dr\Big|\right\}\right)dx',$$

$$(3.2)\qquad \frac{\partial\phi}{\partial t} = -g\zeta - \frac{1}{2\eta^2}\int_{-\infty}^{x}\int_{x}^{\infty}\frac{\phi_{x'}\,\phi_{x''}}{sinh\left(\frac{\pi}{2}\Big|_{x'}\int^{x''}\frac{1}{\eta}dr\Big|\right)}dx''dx'.$$

In order to find wave profiles of constant shape moving with a constant speed, say c (unknown), the following quasi steady state is considered,

$$(3.3)\qquad \zeta(x,t) = \zeta(x-ct) \equiv \zeta(X),$$
$$\phi(x,t) = \phi(x-ct) \equiv \phi(X).$$

Then *(3.1)* and *(3.2)* transform into

$$(3.4)\qquad \frac{d\zeta}{dX} = -\frac{1}{c\pi}\frac{d}{dX}\int_{-\infty}^{\infty}\phi_{X'}\,ln\left(tanh\left\{\frac{\pi}{4}\Big|\int_{X}^{X'}\frac{1}{\eta}dR\Big|\right\}\right)dX' \ ,$$

$$(3.5)\qquad \frac{d\phi}{dX} = \frac{g}{c}\zeta + \frac{1}{2c\eta^2}\int_{-\infty}^{X}\int_{X}^{\infty}\frac{\phi_{X'}\,\phi_{X''}}{sinh\left(\frac{\pi}{2}\Big|_{X'}\int^{X''}\frac{1}{\eta}dR\Big|\right)}dX''dX'.$$

To arrive at a dimensionless form a scaling is performed by means of

$$(3.6)\qquad \tilde{X}=X/h, \quad \tilde{\zeta}=\zeta/h, \quad \tilde{\phi}=\phi/ch.$$

This scaling yields the equations (omitting the tildes)

$$(3.7)\qquad \frac{d\zeta}{dX} = -\frac{1}{\pi}\frac{d}{dX}\int_{-\infty}^{\infty}\phi_{X'}\,ln\left(tanh\left\{\frac{\pi}{4}\Big|\int_{X}^{X'}\frac{1}{1+\zeta}dR\Big|\right\}\right)dX' \ ,$$

$$(3.8)\qquad \frac{d\phi}{dX} = \frac{gh}{c^2}\zeta + \frac{1}{2(1+\zeta)^2}\int_{-\infty}^{X}\int_{X}^{\infty}\frac{\phi_{X'}\,\phi_{X''}}{sinh\left(\frac{\pi}{2}\Big|_{X'}\int^{X''}\frac{1}{1+\zeta}dR\Big|\right)}dX''dX'.$$

In equation *(3.7)* $\frac{d}{dX}$ can be omitted if an unknown constant D is added to the right hand side.

A considerable simplification is obtained if a new variable p is introduced by

$$(3.9)\qquad p(X) = \frac{\pi}{4}\int_{0}^{X}\frac{1}{1+\zeta}dR.$$

This transformation is correct since $1+\zeta$ is positive and assumed to be well-behaved. The transformation of variable leads for the functions $\hat{\zeta}$ and $\hat{\phi}$ defined by

$$(3.10)\qquad \hat{\zeta}(p)=\zeta(X), \qquad \hat{\phi}(p)=\phi(X),$$

to the equations

$$(3.11)\qquad \hat{\zeta}(p) = -\frac{1}{\pi}\int_{-\infty}^{\infty} \hat{\phi}_q \ln(\tanh\{|p-q|\})dq + D,$$

$$(3.12)\qquad \frac{d\hat{\phi}}{dp} = \frac{4gh}{\pi c^2}\hat{\zeta}(1+\hat{\zeta}) + \frac{2}{\pi(1+\hat{\zeta})}\int_{-\infty}^{p}\int_{p}^{\infty} \frac{\hat{\phi}_q\hat{\phi}_r}{\sinh(2(r-q))}drdq.$$

It turns out that these equations can be reduced to a nonlinear integral equation of Hammerstein type. However, attention is paid to the boundary conditions first.

A steady solitary wave solution has vanishing surface elevation at infinity and also the velocity at the surface tends to zero there. In other words, the following boundary conditions hold:

$$(3.13)\qquad \zeta(x,t)\to 0 \quad (x\to\pm\infty), \qquad \frac{\partial\zeta}{\partial x}(x,t)\to 0 \quad (x\to\pm\infty),$$
$$\frac{\partial\phi}{\partial x}(x,t)\to 0 \quad (x\to\pm\infty).$$

If the same transformations as above are carried out, these boundary conditions read as

$$(3.14)\qquad \hat{\zeta}(p)\to 0 \quad (p\to\pm\infty), \qquad \frac{\partial\hat{\zeta}}{\partial p}(p)\to 0 \quad (p\to\pm\infty),$$
$$\frac{d\hat{\phi}}{dp}(p)\to 0 \quad (p\to\pm\infty).$$

With the help of the boundary conditions it is possible to determine the constant D. Since $\hat{\phi}_p(p)\to 0$, $(p\to\pm\infty)$ and the function $\ln(\tanh\{|x|\})$ exhibits a delta function-like behaviour, it can be deduced from $\hat{\zeta}(p)\to 0$, $(p\to\pm\infty)$ and equation *(3.11)* that D must equal zero.

3.3 A nonlinear integral equation.

In order to determine the solutions $\hat{\zeta}$, $\hat{\phi}$ to the equations *(3.11)* and *(3.12)*, it is convenient to simplify the two-dimensional integral in *(3.12)*. To this end, the derivative of the integral with respect to p is taken and the following result is found[1]:

$$(3.15)\qquad \frac{d}{dp}\int_{-\infty}^{p}\int_{p}^{\infty} \frac{\hat{\phi}_q\hat{\phi}_r}{\sinh(2(r-q))}drdq = \frac{\pi}{2}\frac{d\hat{\phi}}{dp}\frac{d\hat{\zeta}}{dp}.$$

Multiplication of *(3.12)* by $(1+\hat{\zeta})$, taking the derivative with respect to p, and applying *(3.15)* yields the equation

[1] *see Appendix I*

(3.16) $$\frac{d^2\hat{\phi}}{dp^2} = \frac{4}{\pi C^2}(1+3\hat{\zeta})\frac{d\hat{\zeta}}{dp} \qquad \left(C \equiv c/\sqrt{gh}\ \text{(Froude number)}\right)$$

which can be integrated to obtain an equivalent of (3.12),

(3.17) $$\frac{d\hat{\phi}}{dp} = \frac{4}{\pi C^2}\hat{\zeta}(1+\frac{3}{2}\hat{\zeta}).$$

It is noted that the equations (3.11) and (3.12) with boundary condition (3.14) now have been replaced by (3.11) and (3.17) with boundary condition (3.14). In fact, the problem has been reduced to the following nonlinear integral equation of Hammerstein type:

(3.18) $$\hat{\zeta}(p) = -\frac{4}{\pi^2 C^2}\int_{-\infty}^{\infty}\hat{\zeta}(q)(1+\frac{3}{2}\hat{\zeta}(q))ln(tanh\{|p-q|\})dq\ ,$$

and a solution $\hat{\zeta}$ is sought which satisfies the condition $\hat{\zeta}(p)\to 0$, $(p\to\pm\infty)$, $\frac{\partial\hat{\zeta}}{\partial p}(p)\to 0$, $(p\to\pm\infty)$.

Not much is known in the literature about the analytical treatment of this type of nonlinear integral equations, and the logarithmic singularity in (3.18) poses additional problems. Therefore, a numerical approach is chosen.

3.4 A numerical approach.

In order to avoid problems with the logarithmic singularity in (3.18), the integral equation is rewritten. The equality

(3.19) $$\int_{-\infty}^{\infty} ln(tanh\{|p-q|\})dq = -\frac{\pi^2}{4}$$

is used to derive the following equivalent of (3.18):

(3.20) $$\hat{\zeta}(p) = \hat{\zeta}(p)(1+\frac{3}{2}\hat{\zeta}(p))/C^2 -$$

$$\frac{4}{\pi^2 C^2}\int_{-\infty}^{\infty}\left[\hat{\zeta}(q)(1+\frac{3}{2}\hat{\zeta}(q))-\hat{\zeta}(p)(1+\frac{3}{2}\hat{\zeta}(p))\right]ln(tanh\{|p-q|\})dq.$$

The integrand in (3.20) behaves well for $q\approx p$, namely like $(p-q)ln(tanh(\{|p-q|\})$.

The appearance of the infinite limits of the integration forms another problem. However, the unknown function $\hat{\zeta}$ has to satisfy boundary condition (3.14), so there exists a real number L such that $|\hat{\zeta}(p)|<\delta$ for all $p\in(-\infty,-L)\cup(L,\infty)$, $\delta\ll 1$. Moreover, $ln(tanh\{|x|\})$ is a rapidly decreasing function for $x\to\pm\infty$. Therefore, it is reasonable to consider the following nonlinear

integral equation instead of *(3.20)*:

$$(3.21)\qquad Z(p) = Z(p)\left(1+\tfrac{3}{2}Z(p)\right)/C^2 - \frac{4}{\pi^2 C^2}\int_{-L}^{L}\left[Z(q)\left(1+\tfrac{3}{2}Z(q)\right)-Z(p)\left(1+\tfrac{3}{2}Z(p)\right)\right]\ln(\tanh\{|p-q|\})dq,\quad p\in[-L,L].$$

Now, the numerical approach is based on successive substitution and discretization in the space variable p. Let N be an integer, $k=L/N$, $p_i=ik$ $(i=-N,...,N)$, $Z_i=Z(p_i)$ $(i=-N,...,N)$, and $\vec{Z}=(Z_{-N},...,Z_N)^t$. Furthermore, let $\vec{Z}^0=(Z^0_{-N},...,Z^0_N)^t$ be a given vector. Application of the repeated trapezoidal rule in order to approximate the integral in *(3.21)* and substitution of $\vec{Z}^0$ into the right hand side of *(3.21)* yields a vector $\vec{Z}^1$. Repetition of this procedure leads to a simple numerical scheme of successive substitution. The choice for the starting vector $\vec{Z}^0$ is based on a theoretical result found by Boussinesq (see §3.5): $Z^0_i=(C^2-1)sech^2\left(\sqrt{3(C^2-1)/4}p_i\right)$ $(i=-N,...,N)$.

Two remarks have to be made here. In the first place, the trivial solution, clearly a solution to *(3.21)*, has to be avoided by the numerical scheme. Secondly, a solution is sought which is symmetric with respect to the origin. The first problem is solved by a scaling of every iteration vector $\vec{Z}^j$. A number $m\in\{1,...,N\}$ is chosen such that Z^0_m hopefully is in the range of the desired function Z and the coordinates $Z^j_{-N},...,Z^j_m$ of the new iteration vector $\vec{Z}^j$ are scaled by a factor Z^{j-1}_m/Z^j_m such that the m-th coordinate of the iteration vector remains unchanged. In this way the iteration vector can adapt to an approximate solution with m-th coordinate Z^0_m. The second problem is solved as follows. Every 10 iteration steps the iteration vector is made symmetric with respect to the origin by means of $Z^j_k:=(Z^j_{-k}+Z^j_k)/2$, $(k=-N,...,N)$. The role of $\vec{Z}^0$ is then taken over by this new vector.

Implementation of the scheme above shows convergence of the iteration vector. The scaling factor converges to *1.0* and the relative distance between two subsequent iteration vectors tends to *0*. In fact, the iteration is stopped if $|Z^{j-1}_m/Z^j_m-1.0|<1.0e\text{-}6$ and $\|\vec{Z}^j-\vec{Z}^{j-1}\|_2/\|\vec{Z}^{j-1}\|_2<1.0e\text{-}6$ and if these conditions are also satisfied after one extra iteration step before which the iteration vector is made symmetric.

The final part of the numerical scheme consists of a transformation of

the approximate solution $\vec{Z}^*$, which approximates $\hat{\zeta}(p)$, into an approximate solution $\vec{\zeta}^*$ to $\zeta(X)$. To this end, the relation $\hat{\zeta}(p)=\zeta(X)$ is used and $X_i = \frac{4}{\pi}\int_0^{p_i}(1+Z(R))dR$ $(i=-N,...,N)$ has to be determined. This is done by means of the repeated trapezoidal rule.

The implemented scheme[2] also computes an approximate solution to the unknown $\hat{\phi}$ by means of formula *(3.17)* and transforms this approximate solution in terms of the original space variable X.

3.5 Results and comparison with the literature.

Some computed results are now presented and compared with results from the literature. Not only wave profiles are studied, but also the amplitude as a function of the Froude number C.

Boussinesq found the following first-order result for the non-dimensional profile η, measured from the bottom (cf. Shields&Webster(1988)).

(3.22) $$\eta(X) = 1 + \alpha[sech^2(\beta X^2)],$$
$$\alpha = C^2-1, \quad \beta^2 = \tfrac{3}{4}\alpha.$$

Laitone found the following second-order result
(cf. Shields&Webster(1988))

(3.23) $$\eta(X) = 1 + \alpha[sech^2(\beta X^2)] + \alpha^2[-\tfrac{3}{4}sech^2(\alpha X)tanh^2(\alpha X)]$$
$$\alpha - \alpha^2/20 = C^2-1, \quad \beta^2 = \tfrac{3}{4}\alpha - 15\alpha^2/16.$$

Williams(1985) gives a large number of tables with results from numerical calculations on the classical equations. Reliable data for solitary waves can be obtained from these tables by looking at very long periodic waves.

In the Figures *3.1(a)-(e)* the interpolated results from the numerical scheme in the previous subsection are plotted. The results have been obtained with $N=150$ and L in the range of *18.0* to *24.0*, dependent on the Froude number C. The corresponding first order approximations of Boussinesq, the second order approximations of Laitone and the results of Williams are also plotted. It has to be mentioned that the tables of Williams only give four or five data points in the interval *[0,7]*. Therefore, these data, which are interpolated by the plotting routine, are explicitly drawn (triangles) in the plots.

The amplitude as a function of the Froude number C is plotted in Figure

[2] *see Appendix II for the source text of the computer program*

3.2 for the different theories.

As already mentioned, there is a maximum to the ratio of amplitude over depth. This implies that it does not make sense to consider Froude numbers greater than *1.3*. It should be mentioned however that the iteration vector $\vec{Z}^j$ in the numerical scheme of the previous subsection still converges for greater Froude numbers. In fact, results are found for Froude numbers up to *5.0*. For greater values of C the iteration vector does not converge. However, this may be caused by the fact that the starting vector is not close enough to a possible solution.

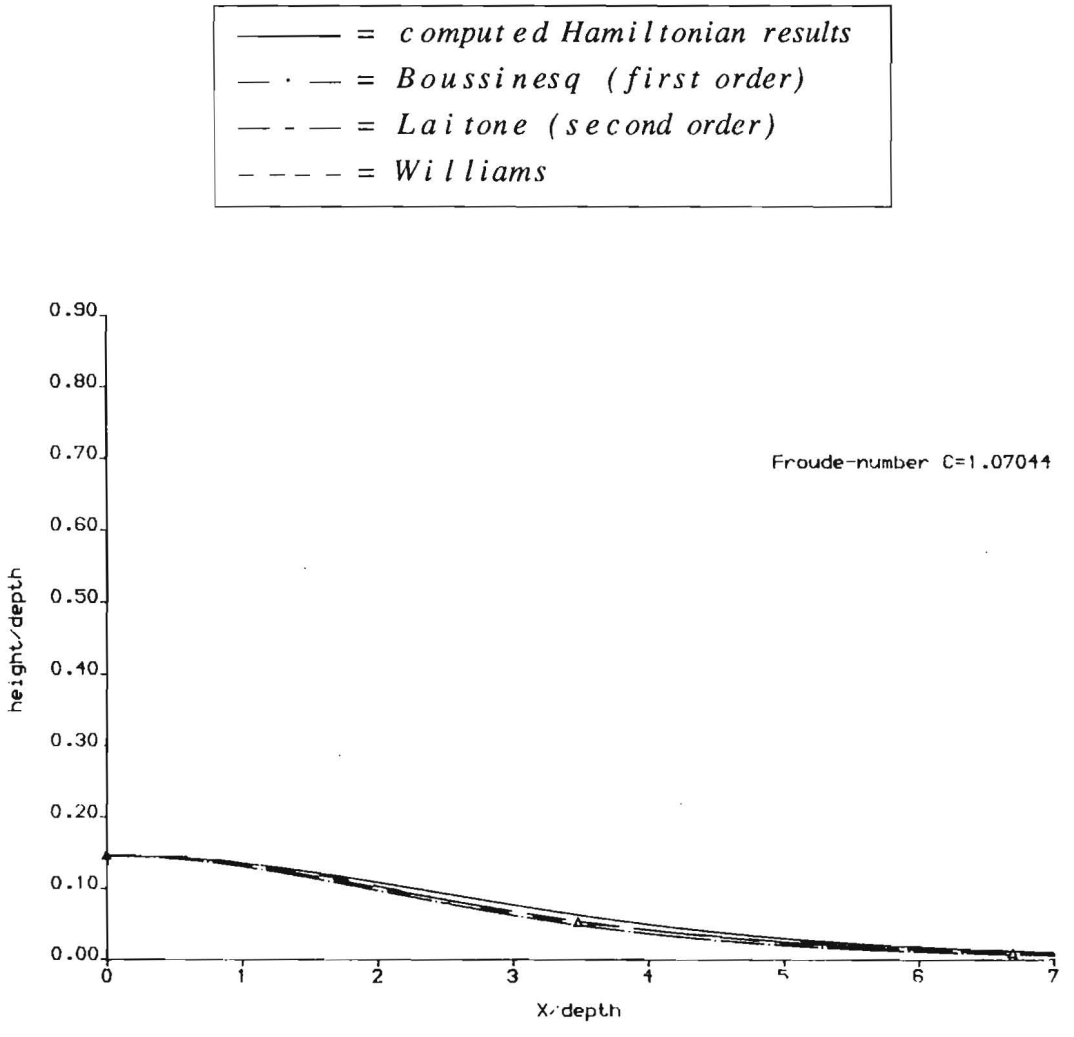

Figure 3.1(a). Surface profile for the solitary wave as predicted by the four theories mentioned in the text.

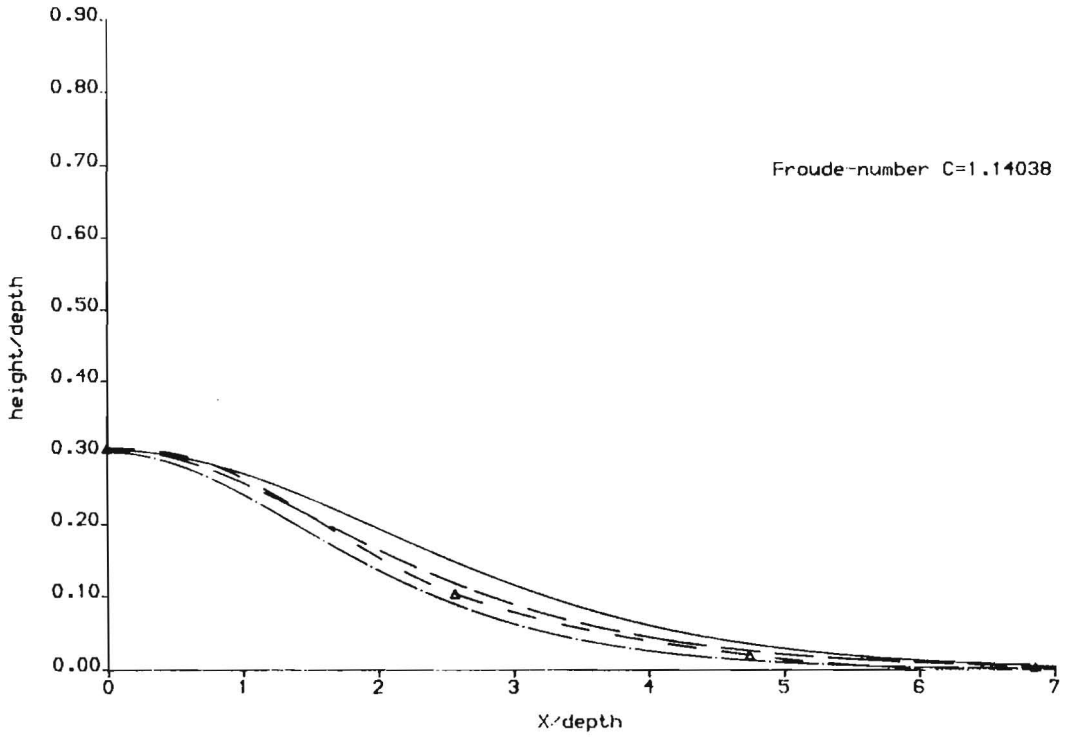

Figure 3.1(b).

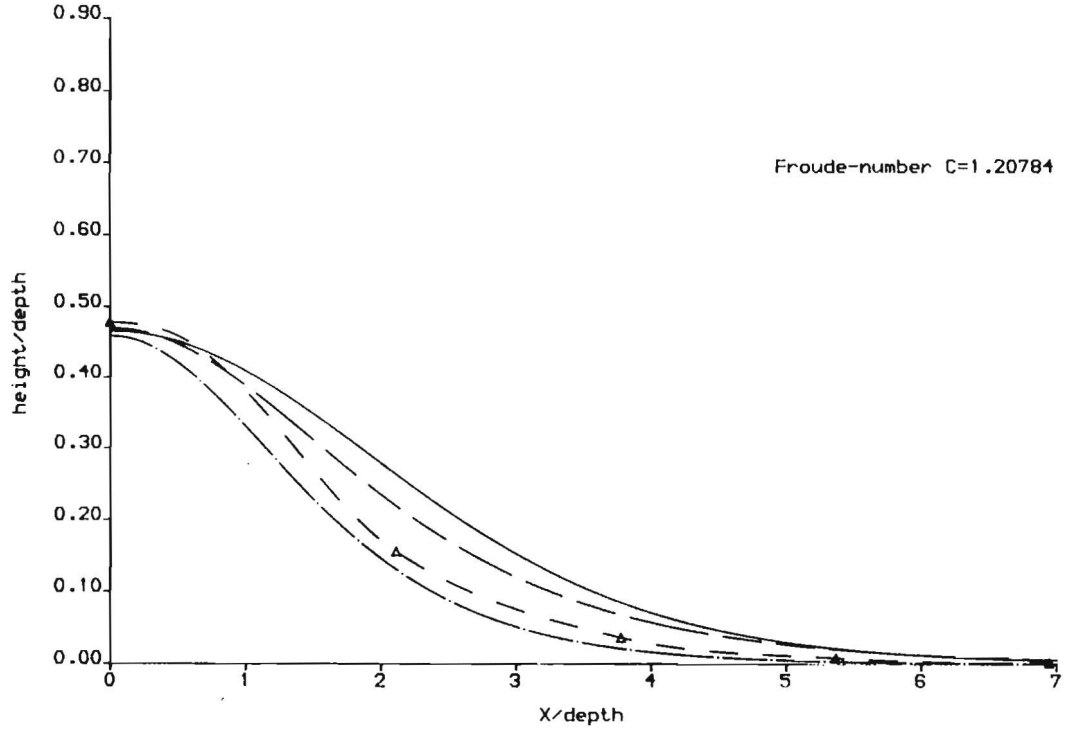

Figure 3.1(c).

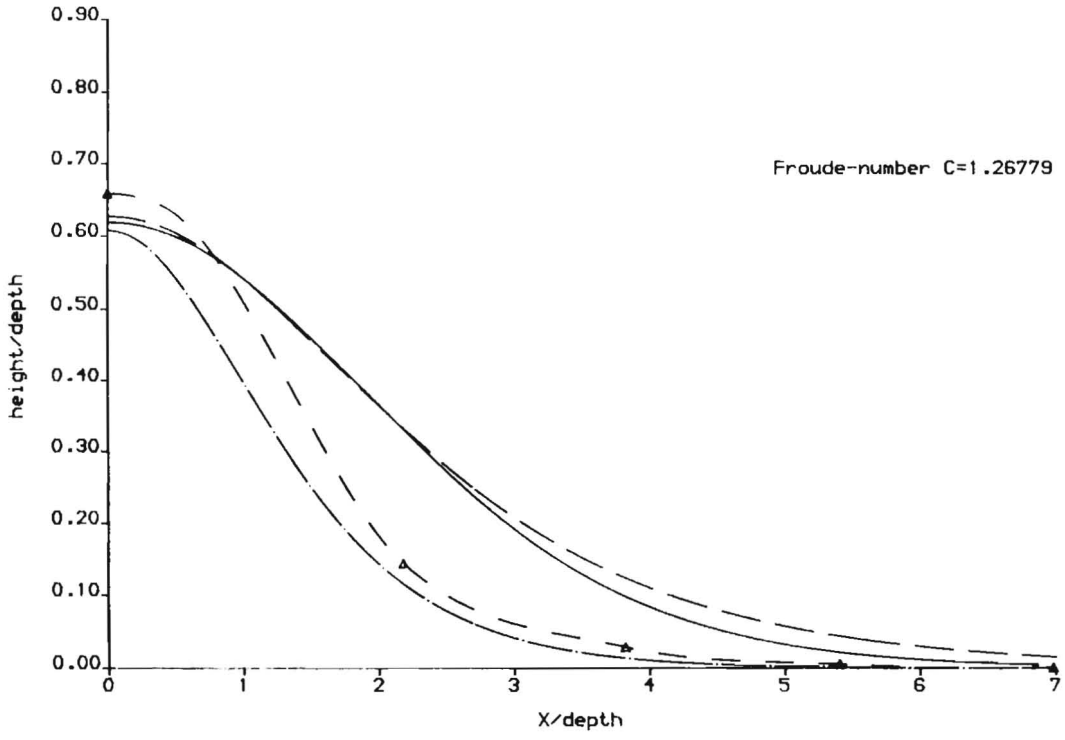

Figure 3.1(d).

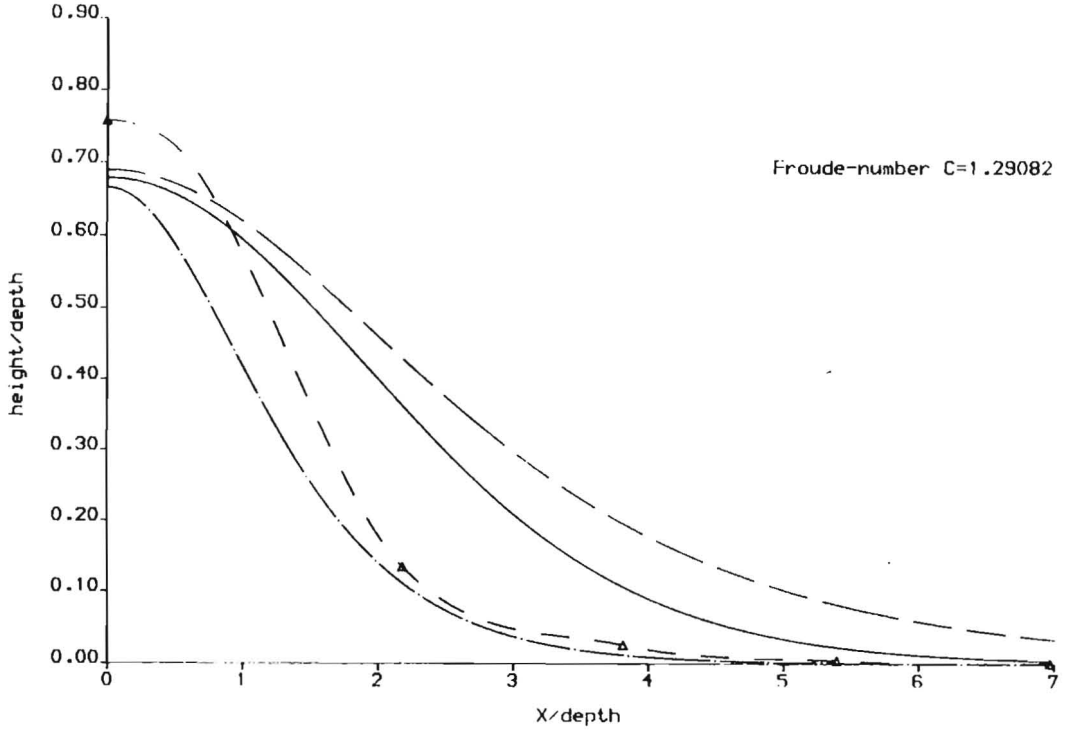

Figure 3.1(e).

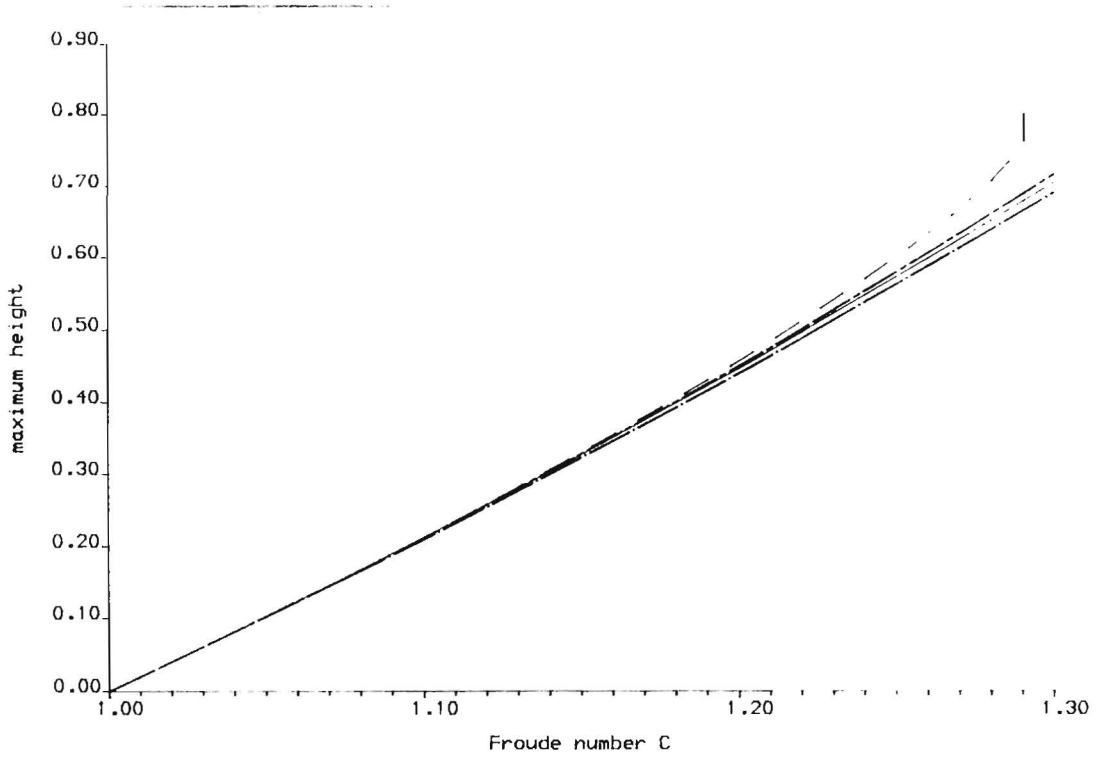

Figure 3.2. Relationship between solitary wave amplitude and Froude number C as predicted by the four theories mentioned in the text.

In Figure *3.1(a)* it can be seen that the results are very similar, although the results from the literature are all slightly lower than the computed Hamiltonian one. The amplitudes of the four approximations are hardly distinguishable.

In Figure *3.1(b)* the computed Hamiltonian result is again above the others. The second order approximation and the Williams result are quite close here. The wave height is again very similar for all four approximations.

Figure *3.1(c)* shows the following. On the one hand, the Boussinesq approximation and the result of Williams are quite similar, and on the other hand, the Laitone approximation and the computed Hamiltonian result are quite similar. This phenomenon is even more striking in Figure *3.1(d)*.

The Froude number of Figure *3.1(e)* already enters the twilight zone in which the theoretically highest possible wave is attained. Again there is a similarity between the first order approximation and Williams' curve, and between the second order result and the computed one.

From Figure *3.2* it can be seen that there is hardly any difference in the amplitudes found for the lower Froude numbers. For greater Froude numbers the computed Hamiltonian solitary wave heights are just in between the first and second order wave heights. For these greater Froude numbers the amplitudes

found by Williams are increasing rather fast to the maximal possible wave height. This phenomenon is not exhibited by the first and second order and the computed Hamiltonian results.

3.6 Summary.

In this section the equations *(3.1)* and *(3.2)* have been reduced to a nonlinear integral equation of Hammerstein type. The nonlinear integral equation is approximately solved by the numerical scheme of § *3.4*. It is concluded that the equations *(3.1)* and *(3.2)* do have solitary wave solutions but a highest solitary wave with a sharp crest and an interior angle of 120° is not found.

Comparison with results from the literature show for the lower Froude numbers a surface profile which is only slightly higher than the other results and for greater Froude numbers a similarity of the computed Hamiltonian results and the second order approximation of Laitone.

It is concluded that neglect of the function $\varepsilon(x)$ in the Hamiltonian functional for the energy density, which in fact causes a neglect of short wave nonlinearity, still leaves a quite good description for low waves. It must be concluded, however, that the description becomes worse for higher waves and that the short wave nonlinearity is indispensable to describe a highest solitary wave with a sharp crest.

4 NUMERICAL TREATMENT OF THE CANONICAL EQUATIONS

This section starts with a discussion of three possible approaches towards a numerical treatment of the equations *(2.12)* and *(2.13)*. One of these approaches is worked out and a numerical scheme is implemented. Several numerical experiments are performed and presented.

4.1 Possible approaches.

The conclusions of the previous section, in which a quasi steady state has been considered, justify a closer look at the dynamical solutions to the canonical equations for two-dimensional wave motion in shallow water.

The development of a numerical scheme to handle these equations serves three goals. First of all, it provides an additional check on the results of the previous section to see whether the computed solitary waves indeed exhibit the expected behaviour. Also, the validity of the model can be examined for an uneven bottom. Finally, general insight may be gained into the possibilities to transform the Hamiltonian description into a a useful computational model for sea waves in coastal regions.

Three ways to come to a numerical treatment are discussed here. One is based on a direct application of the formulas in *(2.6)* and the other two are based on an expansion of the unknown functions in terms of orthonormal basis functions.

Again, the following approximation for the total energy is used

$$(4.1) \qquad \mathcal{H} = \int_{-\infty}^{\infty} \left\{ \tfrac{1}{2} g\zeta^2 - \frac{1}{2\pi} \int_{-\infty}^{\infty} \phi_x \phi_{x'} ln\left(tanh\left\{ \frac{\pi}{4} \left| \int_{x}^{x'} \frac{1}{\eta(r,t)} dr \right| \right\} \right) dx' \right\} dx,$$

where $\eta(x,t) = \zeta(x,t) + h$. A scaling to a dimensionless form is performed by means of

$$(4.2) \qquad \tilde{x} = x/h_0 , \qquad \tilde{t} = t\sqrt{g/h_0} , \qquad \tilde{\phi} = \phi/\sqrt{gh_0^3} , \qquad \tilde{\zeta} = \zeta/h_0 ,$$

$$\tilde{h} = h/h_0 , \qquad \tilde{\eta} = \eta/h_0 , \qquad \tilde{\mathcal{H}} = \mathcal{H}/(gh_0^3) ,$$

where h_0 is a typical depth, e.g., the mean depth. This leads to (omitting the tildes)

$$(4.3) \qquad \mathcal{H} = \int_{-\infty}^{\infty} \left\{ \tfrac{1}{2} \zeta^2 - \frac{1}{2\pi} \int_{-\infty}^{\infty} \phi_x \phi_{x'} ln\left(tanh\left\{ \frac{\pi}{4} \left| \int_{x}^{x'} \frac{1}{\eta} dr \right| \right\} \right) dx' \right\} dx.$$

Now, application of *(2.6)* yields the dimensionless canonical equations for the unknown functions $\zeta(x,t)$ and $\phi(x,t)$ (cf. *(2.12)* and *(2.13)*)

$$\frac{\partial \zeta}{\partial t} = \frac{1}{\pi}\frac{\partial}{\partial x}\int_{-\infty}^{\infty} \phi_x \, ln\left(tanh\left\{\frac{\pi}{4}\Big|\int_x^{x'}\frac{1}{\eta}dr\Big|\right\}\right)dx', \tag{4.4}$$

$$\frac{\partial \phi}{\partial t} = -\zeta - \frac{1}{2\eta^2}\int_{-\infty}^{x}\int_{x}^{\infty}\frac{\phi_x\,,\phi_{x\,,\,,}}{sinh\left(\frac{\pi}{2}\Big|_{x'}\int^{x''}\frac{1}{\eta}dr\Big|\right)}dx''dx'. \tag{4.5}$$

Just as in the previous section, the two-dimensional integral in *(4.5)* is simplified. Determination of the partial derivative with respect to x yields the equation[3]

$$\frac{\partial}{\partial x}\int_{-\infty}^{x}\int_{x}^{\infty}\frac{\phi_x\,,\phi_{x\,,\,,}}{sinh\left(\frac{\pi}{2}\Big|_{x'}\int^{x''}\frac{1}{\eta}dr\Big|\right)}dx''dx' = -2\phi_x\eta\zeta_t\,. \tag{4.6}$$

and with the assumption that $\phi_x \to 0$, $(x\to\pm\infty)$, the following equivalent of *(4.5)* is obtained

$$\phi_t = -\zeta + \frac{1}{\eta^2}\int_{-\infty}^{x}\phi_{x'}\eta\zeta_t dx'\,. \tag{4.7}$$

Since the unknown function ϕ only appears in the form ϕ_x in the right hand sides of *(4.4)* and *(4.7)*, a further simplification is accomplished by taking the partial derivative of *(4.7)* with respect to x. Denoting $v(x,t)=\phi_x(x,t)$ leads to the following system of integro-differential equations for the unknown functions $\zeta(x,t)$ and $v(x,t)$,

$$\zeta_t = \frac{1}{\pi}\frac{\partial}{\partial x}\int_{-\infty}^{\infty} v(x',t)\,ln\left(tanh\left\{\frac{\pi}{4}\Big|\int_x^{x'}\frac{1}{\eta}dr\Big|\right\}\right)dx', \tag{4.8}$$

$$v_t = -\zeta_x - \frac{2}{\eta^3}\eta_x\int_{-\infty}^{x} v(x',t)\eta\zeta_t dx' + (v\zeta_t/\eta)\,. \tag{4.9}$$

The logarithmic singularity in *(4.8)* has to be considered more closely, but a numerical treatment of the equations based on a discretization in space and time is possible. This is the subject of §*4.2*.

However, instead of direct application of the formulas *(2.6)* one can also consider an approach based on an expansion of the unknown functions $\zeta(x,t)$ and $\phi(x,t)$ in terms of orthonormal functions $S_k(x)$, which can be specified later

[3] *see Appendix I*

on:

$$(4.10) \qquad \zeta(x,t) = \sum_k q_k(t)S_k(x) , \qquad \phi(x,t) = \sum_k p_k(t)S_k(x) .$$

The components $q_k(t)$ and $p_k(t)$ satisfy the canonical equations (cf. Miles(1977))

$$(4.11) \qquad \frac{dq_k}{dt} = \frac{\partial \mathcal{H}}{\partial p_k} , \qquad \frac{dp_k}{dt} = - \frac{\partial \mathcal{H}}{\partial q_k} .$$

A spectral description of the wave motion is obtained in the case of a Fourier expansion, i.e., sines and cosines are chosen for the orthonormal functions S_k. In fact, such a description can be very useful since measurements of waves yield data in the form of energy spectra.

It is found that[4]

$$(4.12) \qquad \frac{\partial \mathcal{H}}{\partial p_k} = - \frac{1}{\pi} \int_{-\infty}^{\infty} \frac{dS_k}{dx} \left\{ \int_{-\infty}^{\infty} \phi_{x'} ln\left(tanh\left\{ \frac{\pi}{4} \Big| \int_x^{x'} \frac{1}{\eta} dr \Big| \right\} \right) dx' \right\} dx ,$$

$$(4.13) \qquad - \frac{\partial \mathcal{H}}{\partial q_k} = -q_k - \frac{1}{2} \int_{-\infty}^{\infty} \frac{S_k(x)}{\eta^2(x)} \left\{ \int_{-\infty}^{x} \int_x^{\infty} \frac{\phi_{x'} , \phi_{x''}}{sinh\left(\frac{\pi}{2} \Big|_{x'} \int^{x''} \frac{1}{\eta} dr \Big| \right)} dx'' dx' \right\} dx .$$

In equation *(4.13)* it is just as in *(4.5)* possible to simplify the two-dimensional integral and the equations reduce to

$$(4.14) \qquad \frac{dq_k}{dt} = - \frac{1}{\pi} \int_{-\infty}^{\infty} \frac{dS_k}{dx} \left\{ \int_{-\infty}^{\infty} \phi_{x'} ln\left(tanh\left\{ \frac{\pi}{4} \Big| \int_x^{x'} \frac{1}{\eta} dr \Big| \right\} \right) dx' \right\} dx ,$$

$$(4.15) \qquad \frac{dp_k}{dt} = -q_k + \int_{-\infty}^{\infty} \frac{S_k(x)}{\eta^2(x)} \left\{ \int_{-\infty}^{x} \phi_{x'} \eta \zeta_t dx' \right\} dx .$$

In terms of a Fourier expansion, this is a discretization in the frequency domain. A numerical approach should be based on a reduction of the summation in *(4.10)* to a finite number of indices. Furthermore, a discretization in time is necessary in order to compute approximate solutions to the equations *(4.14)* and *(4.15)*.

In order to avoid the complex equations *(4.14)* and *(4.15)* one might think about a third numerical scheme, which is also based on an expansion like *(4.10)*. Such a scheme consists of a reduction in *(4.10)* to a summation over a

[4] *see Appendix I*

finite number of indices and a direct computation of $\frac{\partial \mathcal{H}}{\partial p_k}$ and $-\frac{\partial \mathcal{H}}{\partial q_k}$ by means of some numerical differencing method. To this end, the total energy $\mathcal{H}$ given by *(4.3)* has to be computed.

All the three approaches should be worked out and studied in more detail to come to a judgement of the accuracy and efficiency of each of the methods. Because such a comparison is not the aim of the present research attention is restricted to the first one.

4.2 A numerical scheme.

The numerical treatment of equations *(4.8)* and *(4.9)* requires the study of the logarithmic singularity in *(4.8)*. This singularity is treated just as in the previous section. The following equality holds[5]:

$$(4.16)\qquad \int_{-\infty}^{\infty} v(x',t)\ln\left(\tanh\left\{\frac{\pi}{4}\left|\int_x^{x'}\frac{1}{\eta}dr\right|\right\}\right)dx' = -\pi\eta(x,t)v(x,t) + \int_{-\infty}^{\infty}\left(v(x',t) - \frac{\eta(x,t)}{\eta(x',t)}v(x,t)\right)\ln\left(\tanh\left\{\frac{\pi}{4}\left|\int_x^{x'}\frac{1}{\eta}dr\right|\right\}\right)dx'.$$

The integrand in the right hand side behaves well in $x'=x$.

Starting point are now the equations

$$(4.17)\qquad \zeta_t(x,t) = \frac{1}{\pi}\frac{\partial}{\partial x}\left(-\pi\eta(x,t)v(x,t) + \int_{-\infty}^{\infty}\left(v(x',t) - \frac{\eta(x,t)}{\eta(x',t)}v(x,t)\right)\ln\left(\tanh\left\{\frac{\pi}{4}\left|\int_x^{x'}\frac{1}{\eta}dr\right|\right\}\right)dx'\right),$$

and

$$(4.18)\qquad v_t(x,t) = -\zeta_x(x,t) - \frac{2}{\eta^3(x,t)}\eta_x(x,t)\int_{-\infty}^{x} v(x',t)\eta\zeta_t dx' + (v\zeta_t/\eta)\ ,$$

with the initial condition

$$(4.19)\qquad \zeta(x,t_0) = \zeta(x)\ , \qquad v(x,t_0) = v(x)\ .$$

Not much can be found in the literature on the numerical treatment of integro-differential equations. Here, a model situation is considered and a simple numerical scheme is developed.

The initial profiles ζ and v are chosen such that they vanish outside a

[5] *see Appendix I*

large interval $0 \leq x \leq L$ and such that the ζ and v profiles remain vanishing on this interval for some time interval $t_0 \leq t \leq t_{end}$. The infinite bounds of integration in *(4.17)* and *(4.18)* can then be replaced by respectively *0* and *L*.

At time $t=t_0$ ζ and v are known by *(4.19)*. Now, for the time derivative in the left hand side of *(4.17)* and *(4.18)* the Euler-forward method is used, i.e., a real number Δt is chosen and a discretization in time is accomplished by

(4.20) $$\zeta^*(x,t_{j+1}) = \zeta^*(x,t_j) + \Delta t\, \zeta^*_t(x,t_j) ,$$

and

(4.21) $$v^*(x,t_{j+1}) = v^*(x,t_j) + \Delta t\, v^*_t(x,t_j) ,$$

where ζ^* and v^* are approximate solutions to ζ and v, and $t_j=t_0+j\Delta t$, $(j\in\mathbb{N})$.

After this, a discretization in space is performed. Let N be an integer, $x_i=iL/N$, $(i=0,...,N)$, $\zeta^*_{i,j}=\zeta^*(x_i,t_j)$, $\vec{\zeta}^*_j=(\zeta^*_{0,j},...,\zeta^*_{N,j})^t$, $v^*_{i,j}=v^*(x_i,t_j)$ and $\vec{v}^*_j=(v^*_{0,j},...,v^*_{N,j})^t$. Then $\zeta^*(x_i,t_{j+1})$ and $v^*(x_i,t_{j+1})$, $(i=0,...,N)$ can be determined with the help of *(4.20)* and *(4.21)* if $\zeta^*_t(x_i,t_j)$ and $v^*_t(x_i,t_j)$, $(i=0,...,N)$ are known. To this end, the right hand sides of *(4.17)* and *(4.18)* are approximated by application of the repeated trapezoidal rule for the integrals and use of the central difference approximation for the derivatives with respect to x. In this way $\vec{\zeta}^*_{j+1}$ and $\vec{v}^*_{j+1}$ are computed as functions of $\vec{\zeta}^*_j$ and $\vec{v}^*_j$.

Despite of the method's apparent simplicity, a theoretical analysis of its behaviour, e.g., concerning stability, looks very hard. Therefore, no theoretical analysis is done but some insight is obtained by means of numerical experiments. Two tests are used here for additional control. Since both conservation of mass and conservation of energy must hold in the continuous problem, the following four quantities are computed:

the mass M^*

(4.22) $$M^*(t_j) = \int_0^L \zeta^*(x,t_j)dx ,$$

the potential energy V^*

(4.23) $$V^*(t_j) = \tfrac{1}{2}\int_0^L (\zeta^*(x,t_j))^2 dx ,$$

the kinetic energy[6] $\mathcal{T}^*$

[6] *see Appendix I*

$$(4.24)\qquad \mathcal{T}^*(t_j) = \tfrac{1}{2}\int_0^L (v^*(x,t_j))^2\eta(x,t_j)dx -$$

$$\tfrac{1}{4\pi}\int_0^L\int_0^L \left\{v^*(x,t_j) - \frac{\eta(x',t_j)}{\eta(x,t_j)}v^*(x',t_j)\right\}\left\{v^*(x',t_j) - \frac{\eta(x,t_j)}{\eta(x',t_j)}v^*(x,t_j)\right\} \cdot$$

$$ln\left(tanh\left\{\left[\frac{\pi}{4}\right| \int_x^{x'} \frac{1}{\eta}dr \left|\right\}\right)dx'dx \ .$$

and the total energy $\mathcal{H}^*$

$$(4.25)\qquad \mathcal{H}^*(t_j) = V^*(t_j) + \mathcal{T}^*(t_j) \ .$$

Again, the repeated trapezoidal rule is used to approximate $M^*(t_j)$, $V^*(t_j)$ and the first term in the right hand side of *(4.24)*. The two-dimensional integral in *(4.24)* is approximated as follows. The integration domain $[0,L]\times[0,L]$ is discretized with a grid of squares. The gridpoints are denoted by (x_i,x_j), $(i,j=0,...,N)$, and the formula

$$(4.26)\qquad \int_{x_i}^{x_{i+1}}\int_{x_j}^{x_{j+1}} f(x,x')dx'dx \approx$$

$$\tfrac{1}{4}(x_{i+1}-x_i)(x_{j+1}-x_j)\,|f(x_i,x_j) + f(x_i,x_{j+1}) + f(x_{i+1},x_j) + f(x_{i+1},x_{j+1})| \ ,$$

is applied. This is equivalent to application of the interpolation formula *(24.2.66)* of Abramowitz&Stegun(1972) to the function f and exact integration.

One final remark is made here. The integral in *(4.7)* is replaced by $\frac{1}{2}\left(\int_{-\infty}^{x} - \int_{x}^{\infty}\right)$ in the implemented scheme[7].

4.3 Numerical experiments.

The results of Section **3** for the solitary wave corresponding to the Froude number $C=1.07044$ are chosen to be the initial values for the first experiment. Furthermore, the following choices are made, $L=100.0$, $N=500$, $\Delta t=0.05$ and $t_0=0.0$. The number of steps in time is *500*, so $t_{end}=25.0$. In Figure *4.1(a)* the results for the surface profile are presented. The lowest, horizontal line represents the bottom and the first line above it is the starting profile. The profile at $t=1.0$ is the first one above the initial profile, the profile at $t=2.0$ is the second one and so on. Every profile

[7] *see Appendix II for the source text of the computer program*

satisfies the condition of rest at the ends of the interval, so, the horizontal ends of each profile correspond to a zero surface elevation.

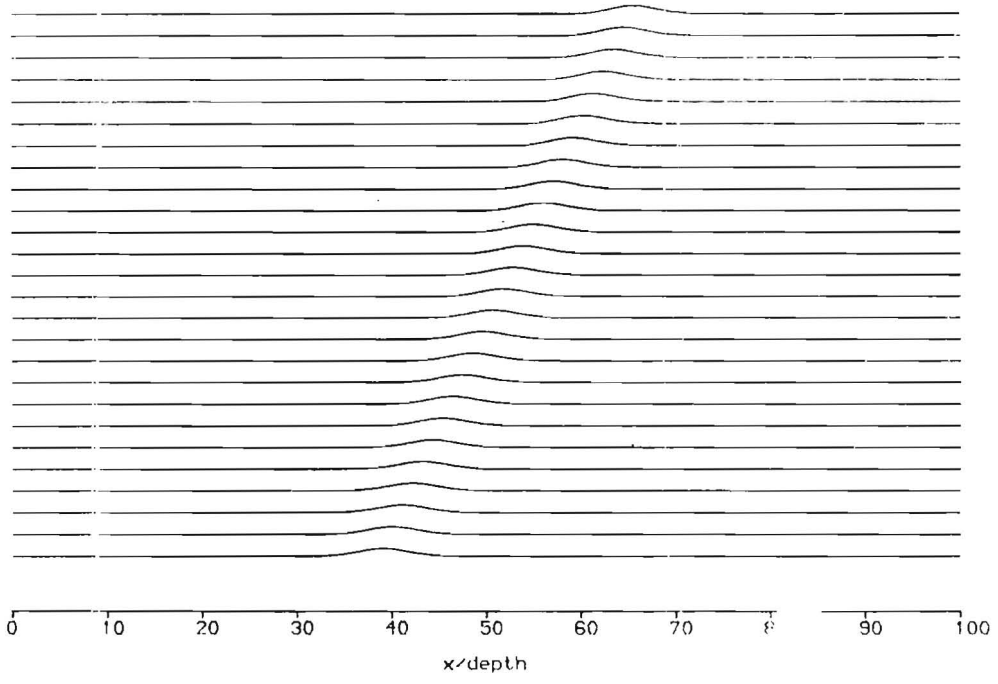

Figure 4.1(a). Evolution of the surface profile (N=500, Δt=0.05, C=1.07044).

Figure *4.1(a)* exhibits the expected behaviour. A single hump of apparently constant form is moving to the right with an apparently constant speed. However, a look at the numerical output shows some features that are hard to distinguish in the graphical output but that should be noticed.

In the first place, the maximum height of the hump and the velocity at the surface of the hump are slowly increasing. In fact, at time $t=0.0$ the surface elevation at the top equals 0.147 and at time $t=24.0$ it equals 0.155, an increase of about 5%. The velocity at the top of the hump grows from 0.136 to 0.155, an increase of no less than 14%.

Moreover, a low wave develops at the left of the hump and moves to the left rather fast, i.e., the solitary hump gets a tail.

Finally, the wave is expected to move with a constant dimensionless speed $C=1.07044$. Here, the top moves from $x=39.09$ at time $t=0.0$ to $x=64.60$ at time $t=24.0$, i.e., it moves with a mean speed of 1.060, a deviation of 1%.

Figure *4.1(b)* shows the results of the additional tests on the conservation of both mass and energy. Here, the horizontal axis represents the time t in the following way: iterationstep m corresponds to $t=m\Delta t$. Table *4.1*

shows some numerical output of these tests. It also gives some results of Williams(1985) for the mass and energy of the solitary wave with Froude number $C=1.07044$.

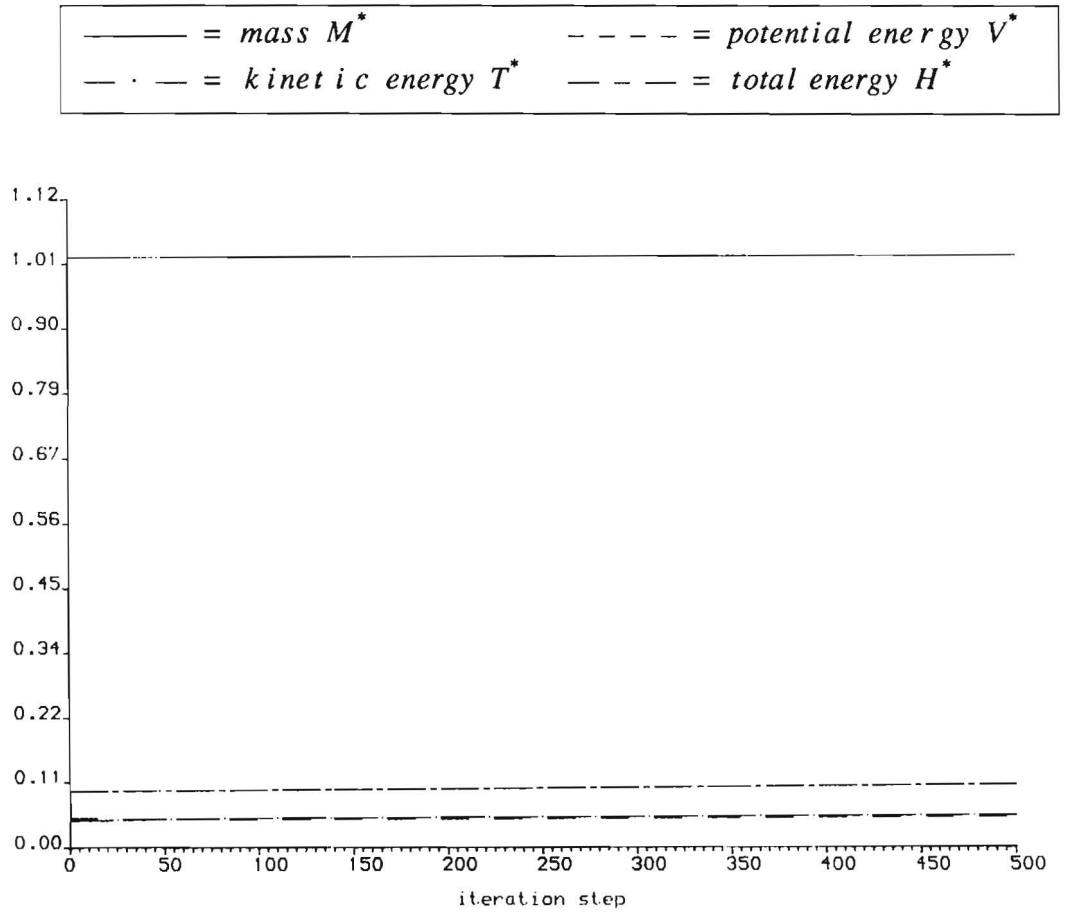

Figure 4.1(b). The evolution of mass, kinetic energy, potential energy and total energy in time (N=500, $\Delta t=0.05$, $C=1.07044$).

	M^*	T^*	V^*	H^*
$t=0.0$	1.0222	0.0465	0.0506	0.0971
$t=25.0$	1.0222	0.0555	0.0526	0.1081
	M	T	V	H
Williams	0.9288	0.0476	0.0452	0.0928

Table 4.1. Numerical output of mass M^*, kinetic energy T^*, potential energy V^*, and total energy H^*, (N=500, $\Delta t=0.05$, $C=1.07044$). Results of Williams for mass M, kinetic energy T, potential energy V and total energy H are given in the last row.

It is clear from Figure *4.1(b)* and Table *4.1* that conservation of mass has been satisfied very well. On the other hand, the total energy increases by about *11%*. The observation that V^* is greater than T^* at time *t=0.0* is rather surprising because other theories predict $T^* \gtrsim V^*$ for solitary waves. One can see in Figure *4.1(b)* that this is satisfied by the computed results only after *60* steps in time. Compared to Williams, the figures resulting from the computations are mostly bigger but this is not unexpected in view of Section **3**.

Although the observed growth of energy is very nice in relation to the world's energy problem, it merely shows the need for further experiments here. Therefore, the same solitary wave is chosen as initial value for a second experiment in which the number of grid points in space has been reduced. *N* is put to *250* and the other parameters have not been changed.

The graphical output of the second experiment is very similar to that of the first and it is omitted here. Again, an increase of the surface elevation at the top of the hump is observed (about *4%*) and an increase of the velocity at the surface of the hump (about *11%* at the top). These increases are a little bit less than before.

The low wave moving to the left is also found here and the mean speed of the top of the hump equals *1.055*.

Table *4.2* shows the results of the additional tests. These are very similar to those of the first experiment. Again, the total energy grows by *11%*.

	M^*	T^*	V^*	H^*
t=0.0	*1.0222*	*0.0465*	*0.0506*	*0.0971*
t=25.0	*1.0222*	*0.0553*	*0.0525*	*0.1078*

Table 4.2. Numerical output of mass M^*, kinetic energy T^*, potential energy V^*, and total energy H^*,(N=250, Δt=0.05, C=1.07044).

In the third experiment the time step Δt is halved to Δt=*0.025* and the number of steps in time is doubled to *1000* so that t_{end} still equals *25.0*. Here, *N=250*.

The graphical output is again very similar to Figure *4.1(a)* and Figure *4.1(b)*. The maximum height of the hump is *0.147* at *t=0.0* and *0.146* at *t=25.0*. The velocity at the top increases by *6%*. The wave tail is found here again and the mean speed of the top is *1.057*.

As a result of the lower top the potential energy is smaller than in the foregoing experiments. Striking is the halving of the energy growth to *5%* (See Table *4.3*).

	M^*	T^*	V^*	H^*
t=0.0	*1.0222*	*0.0465*	*0.0506*	*0.0971*
t=25.0	*1.0222*	*0.0523*	*0.0497*	*0.1020*

Table 4.3. Numerical output of mass M^*, kinetic energy T^*, potential energy V^*, and total energy H^*, ($N=250$, $\Delta t=0.025$, $C=1.07044$).

The time step Δt is halved again in the fourth experiment. Here, $N=250$, $\Delta t=0.0125$, and the number of steps in time is doubled to *2000*. Remarkable is the decrease of the elevation at the top of the hump from *0.147* to *0.142*. The increase of the energy is halved to *2.5%* (see Table *4.4*). Other features are similar to the first three experiments.

	M^*	T^*	V^*	H^*
t=0.0	*1.0222*	*0.0465*	*0.0506*	*0.0971*
t=25.0	*1.0222*	*0.0510*	*0.0484*	*0.0994*

Table 4.4. Numerical output of mass M^*, kinetic energy T^*, potential energy V^*, and total energy H^*, ($N=250$, $\Delta t=0.0125$, $C=1.07044$).

All four experiments are now repeated with the solitary wave corresponding to the Froude number $C=1.14038$ as initial profile. The results are very similar to those found above. The graphical output of the experiment with $N=250$ and $\Delta t=0.0125$ is given in Figure *4.2(a)* and Figure *4.2(b)*.

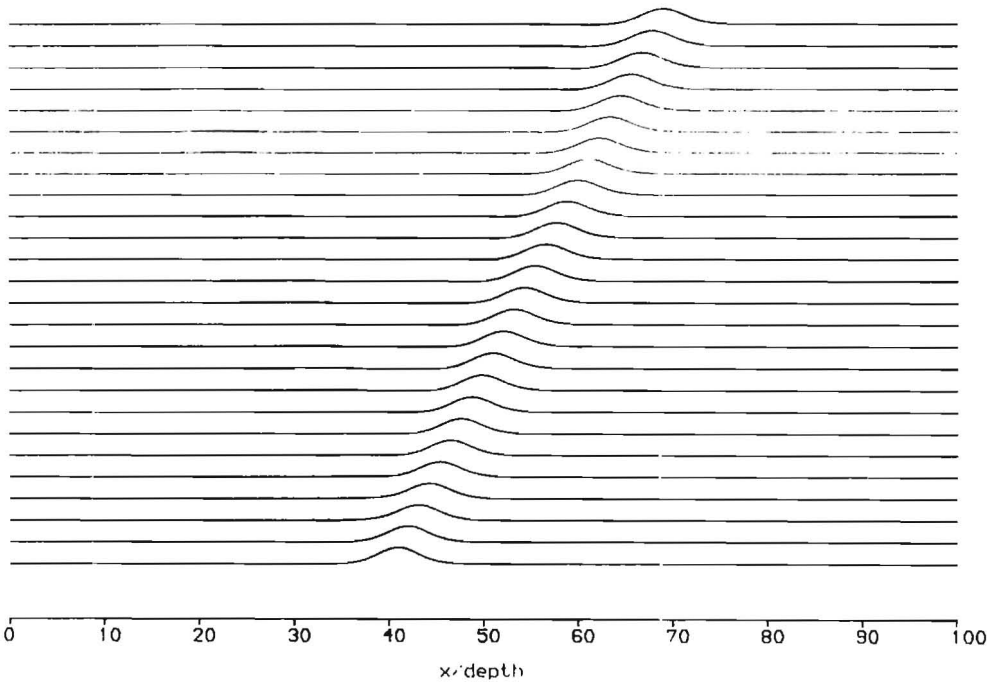

Figure 4.2(a). Evolution of the surface profile (N=250, Δt=0.0125, C=1.14038).

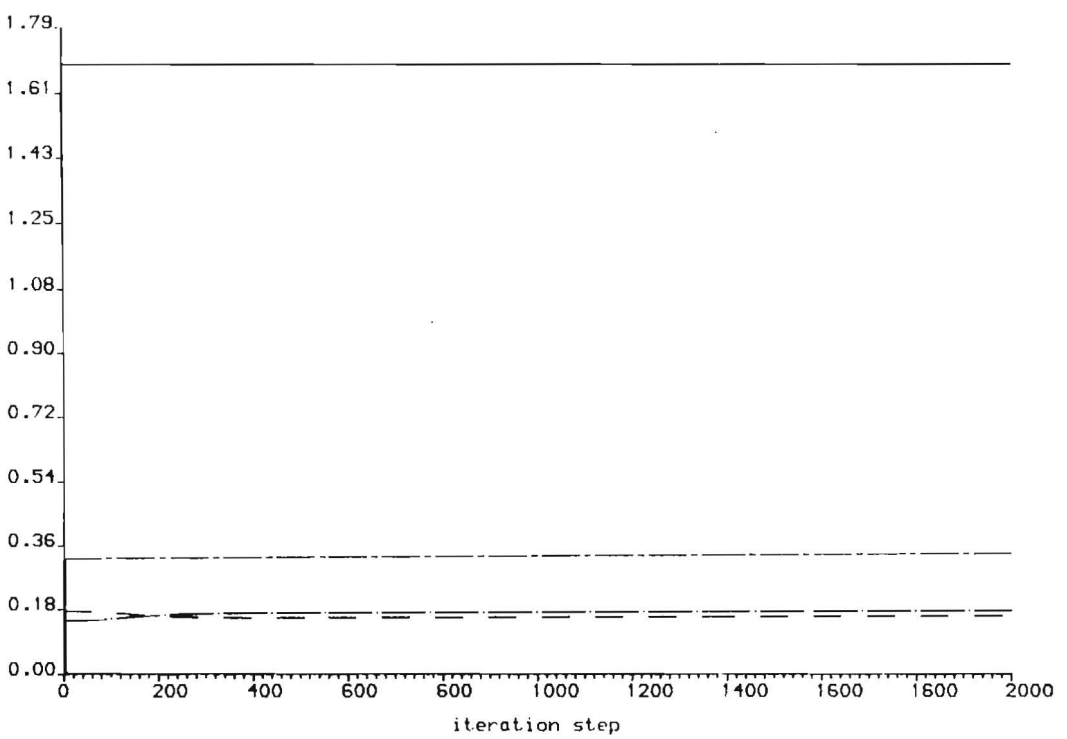

Figure 4.2(b). The evolution of mass, kinetic energy, potential energy and total energy in time (N=250, Δt=0.0125, C=1.14038).

The observations are shortly described here. For $N=500$, $\Delta t=0.05$, the elevation of the top of the hump shows an increase of *7%* and the velocity at the top increases by no less than *23%*. There is a low wave moving to the left again and the mean speed of the top equals *1.1236*, a deviation of *1.5%*. Results for the energy can be found in Table *4.5*. The potential energy is greater than the kinetic energy at $t=0.0$ and the total energy increases by *22%*. Again, the results of Williams are mostly smaller.

	M^*	T^*	V^*	H^*
$t=0.0$	1.6928	0.1480	0.1754	0.3234
$t=25.0$	1.6928	0.2072	0.1880	0.3952
	M	T	V	H
Williams	1.3877	0.1535	0.1390	0.2925

Table 4.5. Numerical output of mass M^*, kinetic energy T^*, potential energy V^*, and total energy H^*, ($N=500$, $\Delta t=0.05$, $C=1.14038$). Results of Williams for mass M, kinetic energy T, potential energy V and total energy H are given in the last row.

For $n=250$ and $\Delta t=0.05$, the phenomena are so similar that only the results for the mass and energy are presented in Table *4.6*.

	M^*	T^*	V^*	H^*
$t=0.0$	1.6928	0.1480	0.1754	0.3234
$t=25.0$	1.6928	0.2047	0.1861	0.3908

Table 4.6. Numerical output of mass M^*, kinetic energy T^*, potential energy V^*, and total energy H^*, ($N=250$, $\Delta t=0.05$, $C=1.14038$).

In the case of halving the time step to respectively $\Delta t=0.025$ and $\Delta t=0.0125$ the main features that have to be mentioned are the lower potential energy and the decrease of the energy growth to respectively *9%* and *4.5%*. Tables *4.7* and *4.8* contain the results for mass and energy.

	M^*	T^*	V^*	H^*
$t=0.0$	1.6928	0.1480	0.1754	0.3234
$t=25.0$	1.6928	0.1846	0.1686	0.3531

Table 4.7. Numerical output of mass M^*, kinetic energy T^*, potential energy V^*, and total energy H^*, ($N=250$, $\Delta t=0.025$, $C=1.14038$).

	M^*	T^*	V^*	H^*
$t=0.0$	1.6928	0.1480	0.1754	0.3234
$t=25.0$	1.6928	0.1761	0.1613	0.3374

Table 4.8. Numerical output of mass M^*, kinetic energy T^*, potential energy V^*, and total energy H^*, ($N=250$, $\Delta t=0.0125$, $C=1.14038$).

In all experiments, conservation of mass is extremely well satisfied.The increase of energy is a rather unpleasant feature but it is observed that the energy growth halves when the time step Δt is halved.

The observations that the initial profiles do not exactly behave as solitary waves can have several causes. First of all, the phenomenon that $V^* \gtrsim \mathcal{I}^*$ at time $t=0.0$ and that only after a number of steps in time $V^* \lesssim \mathcal{I}^*$ as predicted by other theories seems to indicate that the initial profiles are not exactly solitary waves. This can be a result of rounding and discretization errors in Section **3** but also of the interpolation of the results of Section **3** to obtain the desired initial values here. Secondly, discretization errors and rounding errors in the numerical scheme might be a cause. A theoretical analysis of the numerical method could yield useful information on this subject but is difficult.

The effect of the number of grid points in space is hard to judge. The profiles considered here are rather smooth and no real distinction is found between the results for $N=500$ and for $N=250$.

The general insight obtained by the experiments is that the choice of the time step Δt is quite important.

4.4 Two more experiments.

Two more experiments are done. In the first place, an initial profile of a single hump with zero velocity at the surface is considered. The following choices are made, $L=80.0$, $N=250$, $\Delta t=0.02$ and $t_{end}=20.0$. The results are presented in Figure *4.3(a)*, Figure *4.3(b)* and Table *4.9*.

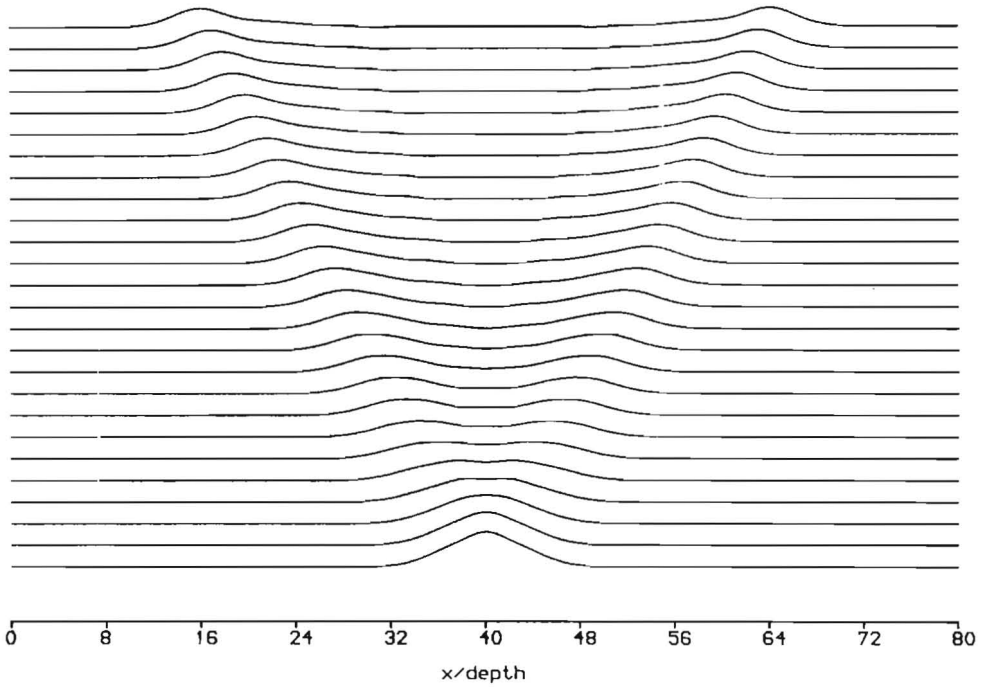

Figure 4.3(a). The evolution of the profile of a single hump with zero velocity at the surface at t=0.0, (N=250, Δt=0.02).

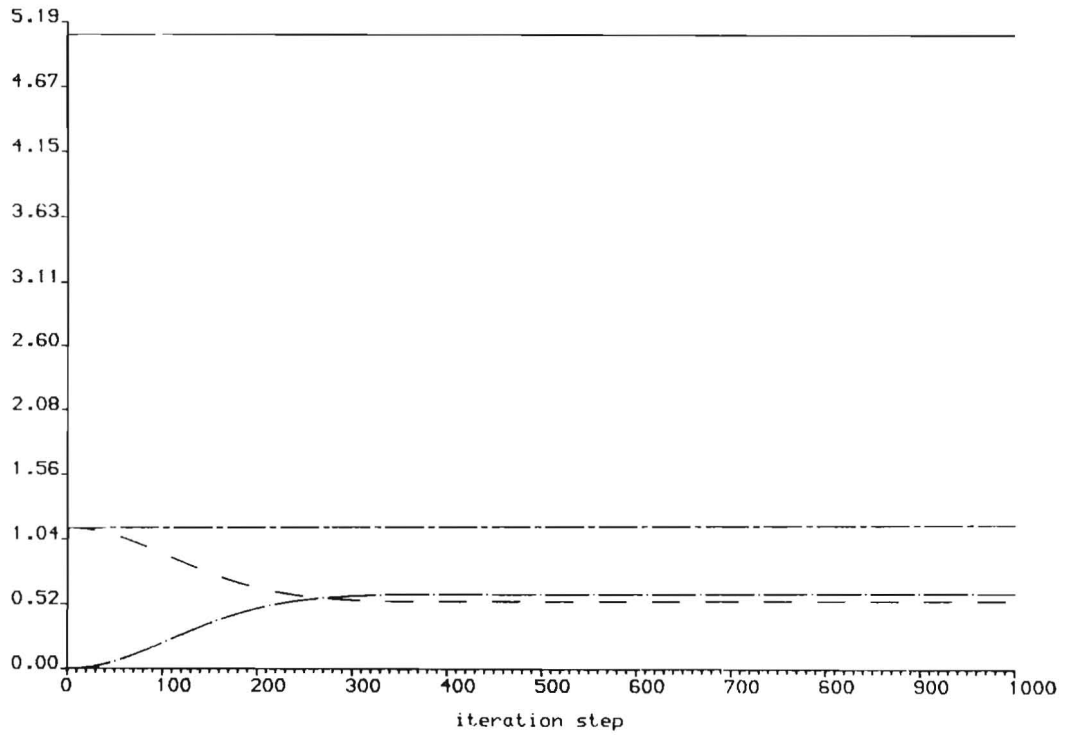

Figure 4.3(b). The evolution of mass, kinetic energy, potential energy and total energy in time (N=250, Δt=0.02).

	M^*	T^*	V^*	H^*
$t=0.0$	5.0904	0.0000	1.1302	1.1302
$t=20.0$	5.0904	0.6127	0.5528	1.1655

Table 4.9. Numerical output of mass M^*, kinetic energy T^*, potential energy V^*, and total energy H^*, ($N=250$, $\Delta t=0.02$).

As a result of gravity, the single hump in Figure *4.3(a)* falls apart into two equal single humps, one moving to the left and one moving to the right. More than half of the potential energy is converted into kinetic energy (see Figure *4.3(b)*). The mass is perfectly conserved and the increase of the total energy is only *3%*.

The second experiment is concerned with two solitary waves travelling in opposite directions (see Figure *4.4(a)*). The left wave in the initial profile corresponds to $C=1.10$ and the right one to $C=1.15$. Here, $L=150.0$, $N=500$, $\Delta t=0.02$ and $t_{end}=37.7$. The results are presented in Figure *4.4(a)*, Figure *4.4(b)* and Table *4.10*.

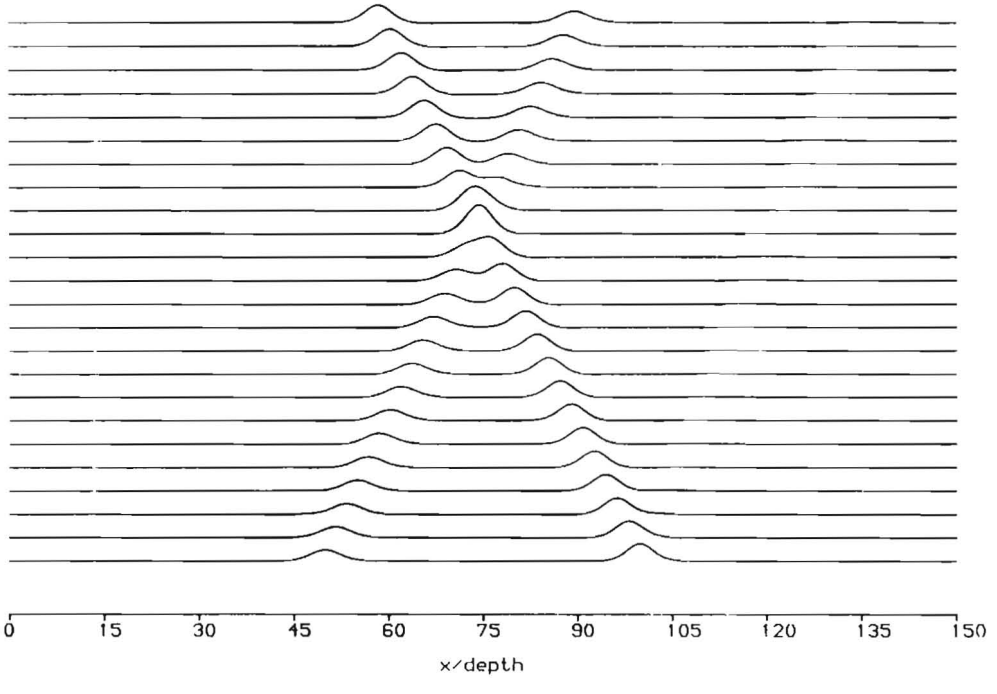

Figure 4.4(a). Two solitary waves travelling in opposite directions ($N=500$, $\Delta t=0.02$).

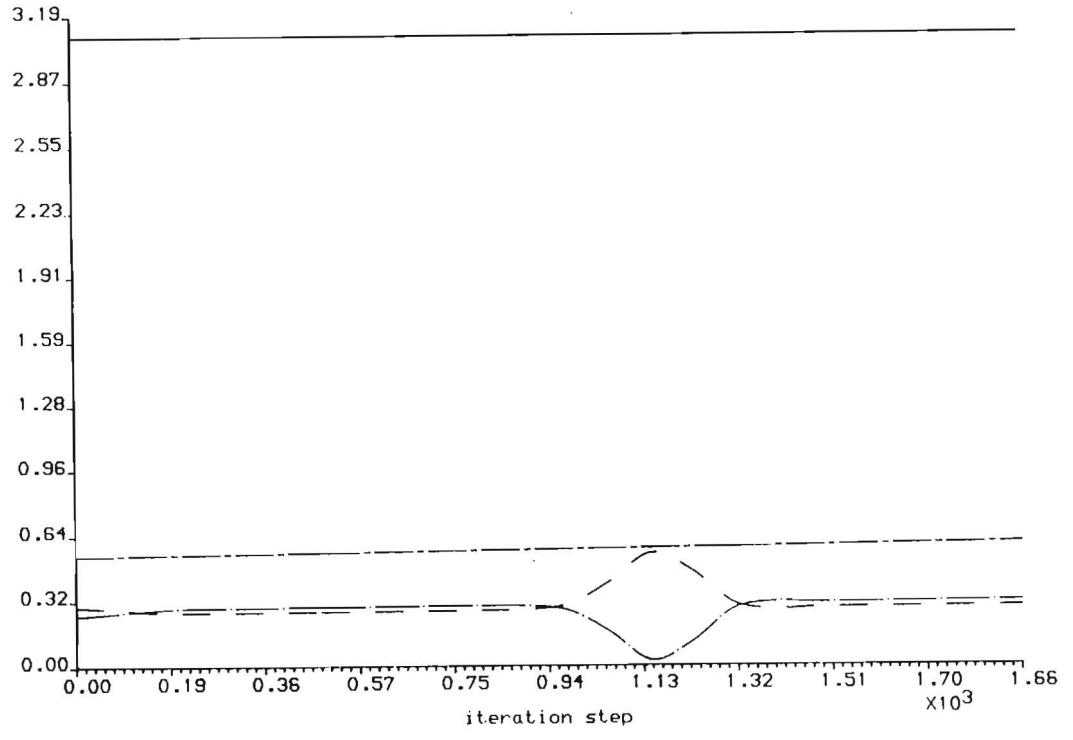

Figure 4.4(b). The evolution of mass, kinetic energy, potential energy and total energy in time (N=500, Δt=0.02).

	M^*	T^*	V^*	H^*
$t=0.0$	3.0893	0.2489	0.2926	0.5415
$t=37.7$	3.0891	0.3120	0.2858	0.5978

Table 4.10. Numerical output of mass M^*, kinetic energy T^*, potential energy V^*, and total energy H^*, (N=500, Δt=0.02).

The two waves travel on after the meeting just as if nothing has happened. The heights of the two humps are almost constant in time. From Figure *4.4(b)* it can be seen that during the meeting almost all kinetic energy is converted into potential energy. Again, conservation of mass holds but the total energy increases by an amount of *10%*.

4.5 Submerged obstacles.

Two final experiments are presented here as a first step towards a judgement of the validity of the model when the bottom is not horizontal. In this case h is replaced by $h(x)$ in the equations *(4.16)* and *(4.17)*.

The first experiment deals with a submerged breakwater with a height of

0.45 (see Figure *4.5(a)*). A similar obstacle of height *0.6* appears in Takashi&Masanori(1990). However, Takashi&Masanori(1990) deals with the phenomenon of breaking and it makes no sense to compare results.

The Froude number C equals *1.1818* here, $L=100.0$, $N=400$, $\Delta t=0.025$, and $t_{end}=25.0$. The graphical output is in Figure *4.5(a)* and Figure *4.5(b)*. It can be seen in Figure *4.5(a)* that instabilities develop when the top of the hump passes the edges of the submerged obstacle. At time $t=21.0$ the surface profile even becomes almost vertical. Another feature can be seen at the left of the instabilities. A low wave is reflected by the obstacle when the hump passes it. This low wave moves to the left.

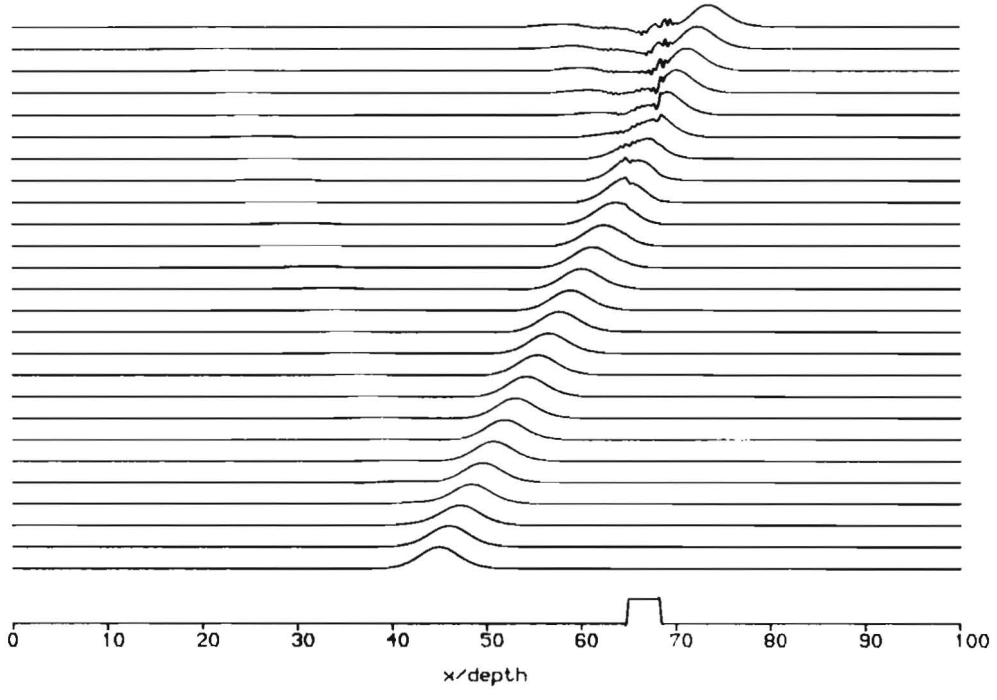

Figure 4.5(a). Evolution of the surface profile when a solitary wave passes a submerged obstacle of height 0.45, ($N=400$, $\Delta t=0.025$, $C=1.1818$).

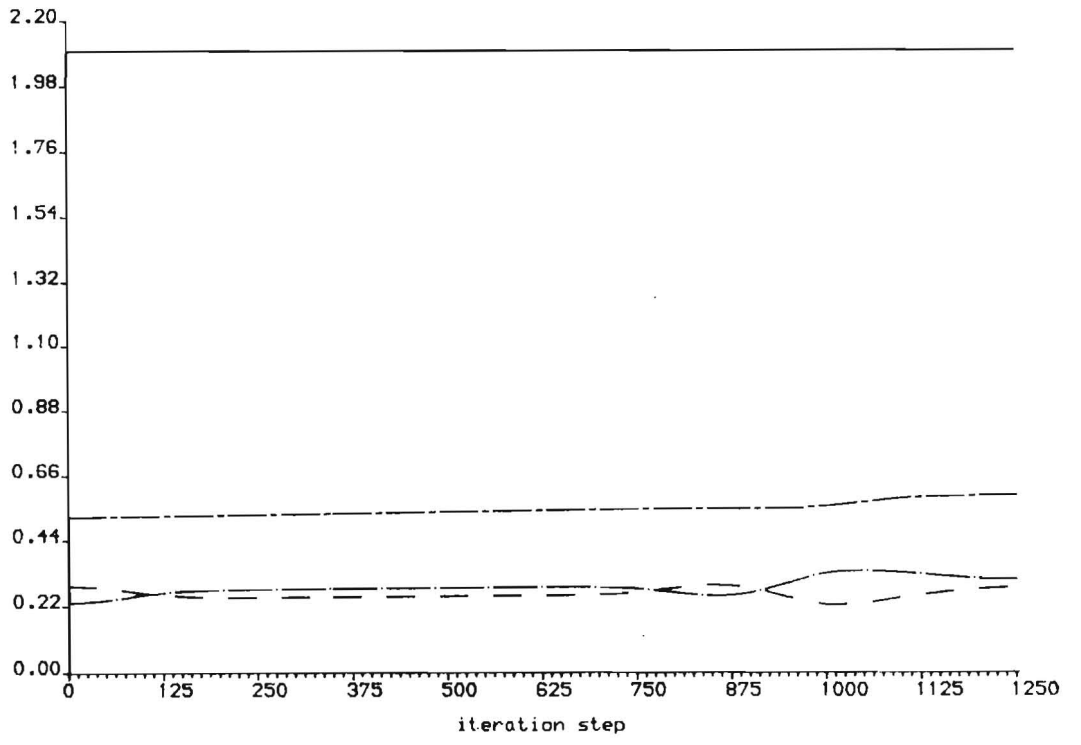

Figure 4.5(b). The evolution of mass, kinetic energy, potential energy and total energy in time (N=400, Δt=0.025, C=1.1818).

Although conservation of mass is satisfied very well (see Figure *4.5(b)*), it is observed that conservation of energy is spoiled when the solitary wave passes the breakwater. Other experiments with lower breakwaters show slightly better results but it must be concluded that the numerical scheme does not give reliable results for such a steep submerged obstacle.

The second experiment is concerned with a high but smooth submerged obstacle (see Figure *4.6(a)*). The height of the obstacle is *0.6*. The following choices are made: *C=1.1818*, *L=100.0*, *N=400*, *Δt=0.2* and t_{end}*=30.0*. The graphical output is in Figure *4.6(a)* and Figure *4.6(b)*.

When the top of the hump passes the obstacle, the amplitude increases and the single hump falls apart into three separate humps. No instabilities occur, even though the obstacle is even higher than in the previous experiment. In real life, the wave is expected to break. Again, a low wave is reflected and moves to the left. There is a resemblance with an undular bore.

Figure *4.6(b)* shows that conservation of energy is satisfied. As expected, the potential energy decreases and the kinetic energy increases during the passing of the obstacle. The total energy grows by *14%* but this is expected to be lower for a smaller time step.

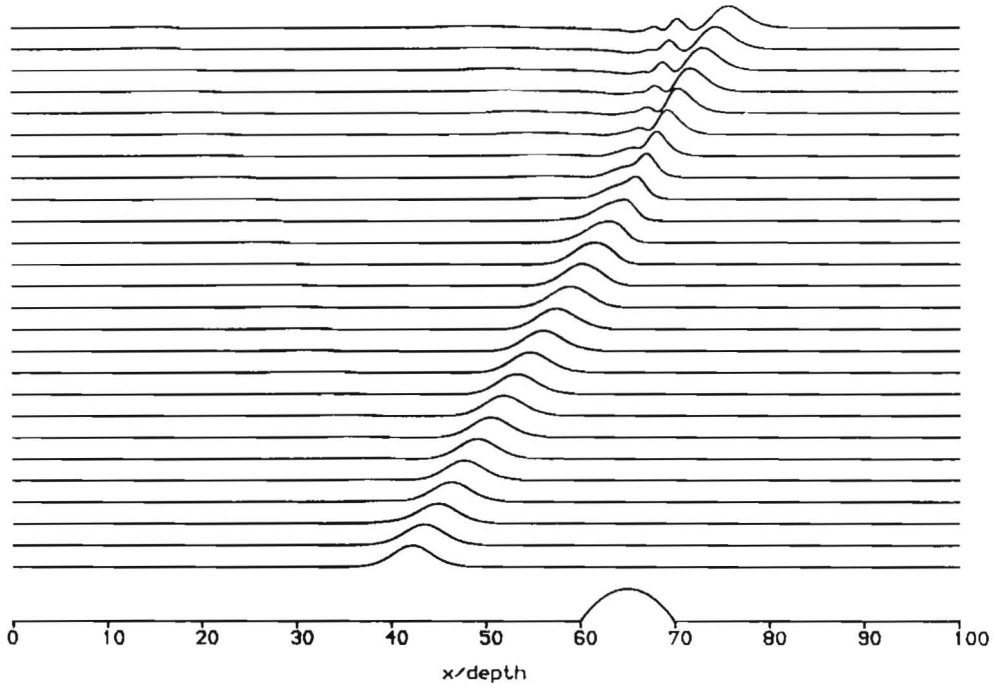

Figure 4.6(a). Evolution of the surface profile when a solitary wave passes a submerged obstacle of height 0.6, (N=400, Δt=0.2, C=1.1818).

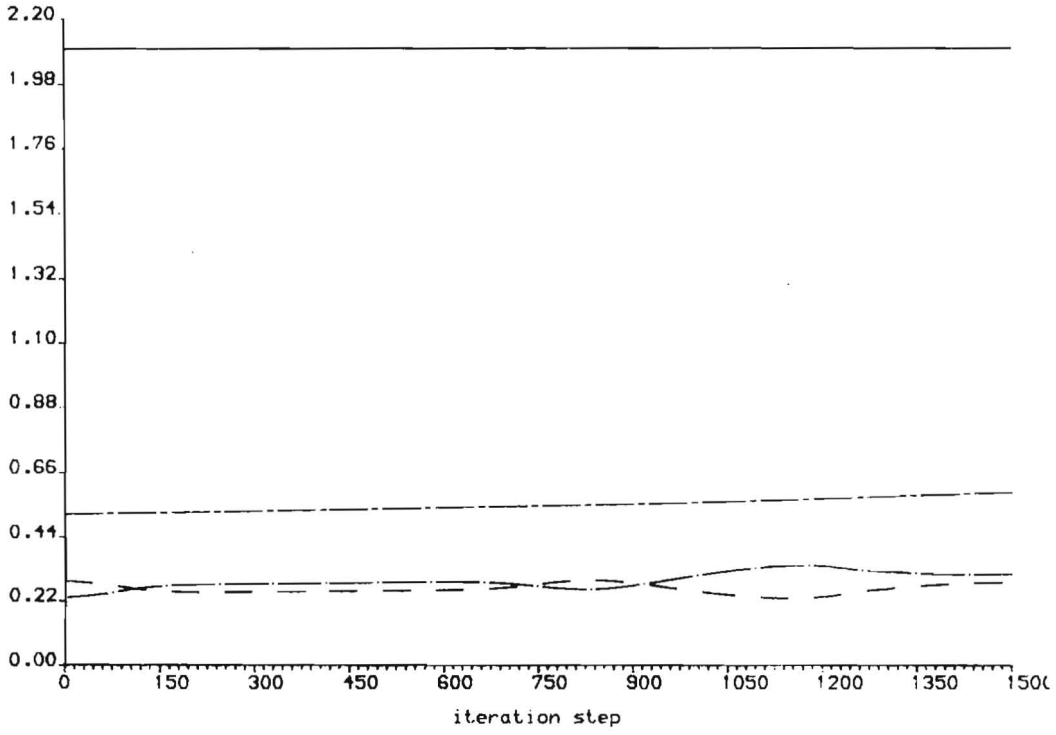

Figure 4.6(b). The evolution of mass, kinetic energy, potential energy and total energy in time (N=400, Δt=0.02, C=1.1818).

4.6 Summary.

Three ways to tackle the canonical equations for two-dimensional wave motion have been discussed. The first one is worked out in a simple numerical scheme and implemented. Experiments show reasonable results if the time step is carefully chosen. Conservation of mass is satisfied very well by this scheme, even in the case of a submerged obstacle. The total energy shows an increase which is a rather unpleasant feature. However, this growth is clearly dependent on the time step Δt and it is observed that the growth of energy halves when the time step is halved.

The solitary waves of the previous section do not exactly show the expected behaviour. It is observed that $\mathcal{T}^* < V^*$ at time $t=0.0$ and this does not correspond to other theories.

The scheme also works for a bottom with an obstacle. However, instabilities occur for a very steep submerged obstacle.

5 CONCLUSIONS

The canonical equations in §*2.4*, which are derived from a straightforward approximation of the Hamiltonian density in shallow water, have solitary wave solutions. For the lower Froude numbers ($C \leq 1.10$) these solutions are similar to results from the literature found by Boussinesq, Laitone and Williams. For the higher Froude numbers ($1.10 < C < 1.3$) there is a similarity to the results of Laitone. A highest solitary wave is not found. It is concluded that inclusion of short wave nonlinearity is indispensable to describe such a highest wave.

For the description of solitary waves, the canonical equations can be tackled by a simple numerical scheme based on a discretization in space (equidistant grid, repeated trapezoidal rule and central differences) and time (Euler-forward). The method appears to be quite sensitive for the choice of the time step. Therefore, it might be worthwhile to implement a method more accurate than Euler-forward. The present numerical scheme also works for an uneven bottom. Further research is necessary to judge the results for such an uneven bottom and to understand the effect of the number of gridpoints in space.

REFERENCES

BROER, L.J.F. 1974
On the Hamiltonian theory of surface waves.
Appl. Sci. Res. **29**, 430-446.

BROER, L.J.F. 1975
Approximate equations for long water waves.
Appl. Sci. Res. **31**, 377-395.

BROER, L.J.F. & GROESSEN, E.W.C. & TIMMERS, J.M.W. 1976
Stable model equations for long water waves.
Appl. Sci. Res. **32**, 619-636.

FENTON, J.D. & RIENECKER, M.M. 1982
A Fourier method for solving nonlinear water-wave problems: application to solitary wave interactions.
J. Fluid Mech. **118**, 411-443.

HUNTER, J.K. & VANDEN-BROECK, J.M. 1983
Accurate computations for steep solitary waves.
J. Fluid Mech. **136**, 63-72.

LONGUET-HIGGINS, M.S. & COKELET, E.D. 1976
The deformation of steep surface waves on water I. A numerical method of computation.
Proc. R. Soc. Lond. **A350**, 1-26.

MEI, C.C. 1989
The applied dynamics of ocean surface waves.
Wiley, New York.

MILES, J.W. 1977
On Hamilton's principle for surface waves.
J. Fluid Mech. **83**, 153-158.

MURRAY, R. 1988
A numerical wave model based on new equations of Boussinesq type which incorporate improved dispersion characteristics.
Report Series no. 18, Int. Inst. Hydr. & Envir. Eng. Delft.

RADDER, A.C. 1991
An explicit Hamiltonian formulation of surface waves in water of finite depth.
submitted for publication.

SHIELDS, J.J. & WEBSTER W.C. 1988
On direct methods in water-wave theory.
J. Fluid Mech. **197**, 171-199.

TAKASHI, Y. & MASANORI, H.
Breaking and reflection of a steep solitary wave caused by a submerged obstacle.
Proceedings ICCE '90, Delft.

WHITHAM, J.M. 1967
Variational methods and applications to water waves.
Proc. R. Soc. Lond. **A229**, 6-25.

WHITHAM, J.M. 1974
Linear and nonlinear waves.
Wiley, New York.

WILLIAMS, J.M. 1985
Tables of progressive gravity waves.
Pitman, London.

WITTING, J.M. 1984
A unified model for the evolution of nonlinear water waves.
J. Comput. Phys. **56**, 203-236.

ZAKHAROV, V.E. 1968
Stability of periodic waves of finite amplitude on the surface of a deep fluid.
J. Appl. Mech. Tech. Phys. **2**, 190-194.